

Leveraging TROPOMI observations and WRF-GHG modeling ~~to improve~~ towards improving methane emission assessments in India

Thara Anna Mathew^{1,2}, Dhanyalekshmi Pillai^{1,2}, Jithin Sukumaran^{1,2}, Monish Vijay Deshpande^{1,2,3}, Michael Buchwitz⁴, Oliver Schneising⁴, Vishnu Thilakan^{1,2,5}, Aparna Ravi^{1,2}, Sanjid Backer Kanakkassery^{1,2,6}, Sivarajan Sijikumar⁷, Imran A Girach⁸, and S Suresh Babu⁷

¹Indian Institute of Science Education and Research Bhopal (IISERB), India

²Max Planck Partner Group (IISERB), Max Planck Society, Munich, Germany

³Now at the University of Michigan, Ann Harbor, Michigan, USA

⁴Institute of Environmental Physics (IUP), University of Bremen FB1, Bremen, Germany

⁵Now at Lund University, Lund, Sweden

⁶Now at Max Planck Institute for Biogeochemistry (MPI-BGC), Jena, Germany

⁷Space Physics Laboratory (SPL), Vikram Sarabhai Space Centre, Thiruvananthapuram, India

⁸Space Applications Centre (SAC), Indian Space Research Organization, Ahmedabad, India

Correspondence: Dhanyalekshmi Pillai (dhanya@iiserb.ac.in)

Abstract.

Atmospheric methane (CH₄) contributes to global warming and climate change. Multiple factors control its atmospheric growth rate, posing challenges for climate change mitigation in regions with limited observations, like India. In this study, we examine the potential of dry air column methane mixing ratio (XCH₄) observations from the Tropospheric Monitoring Instrument (TROPOMI) in conjunction with the high-resolution Weather Research ~~Forecast and Forecasting~~ model with Greenhouse Gas module (WRF-GHG) to improve the annual CH₄ budget of India. In addition to an inversion framework, we present a spatiotemporal assessment of bottom-up Indian methane emissions and their influence on XCH₄, supplying the context needed for regional emission optimization. Our analysis demonstrates the potential of WRF-GHG to represent the atmospheric XCH₄ and CH₄ distributions, including seasonal patterns, albeit with non-negligible uncertainties when compared with satellite and ground-based observations for 2018 and 2019. We find that the WRF-GHG simulations ~~overestimate the XCH₄ and underestimate the~~ tend to overestimate XCH₄ while underestimating near-surface CH₄ ~~distributions. Our first-order concentrations at the Thumba site. Our~~ inversion analyses report annual CH₄ emissions ranging from 23.3 to 25.2 Tg with an uncertainty of 3.3 Tg (anthropogenic sources), ~~showing that the current global emission inventories overestimate CH₄ emissions considerably. Our~~ implying an overestimation of 14 to 20 % by the EDGAR global inventory. Also, our estimates are approximately 19 % higher than those in the India Fourth Biennial Update Report (19.6 Tg) and close to the latest Global Methane Budget 2000-2020 (~~21.7 Tg~~). Overall, this study demonstrates the usefulness of TROPOMI observations for assessing Indian CH₄ emissions and shows a way to improve our understanding of how regional processes can modulate atmospheric CH₄ mixing ratios. We highlight the need for expanded observational coverage and an improved carbon assimilation system over India to refine the methane budget in support of global climate goals.

20 1 Introduction

The concentration of atmospheric CO₂ has increased by ~~nearly more than~~ 50 % of the pre-industrial levels, while that of CH₄ has increased by 150 % (~~Ciais et al., 2014; Myhre et al., 2013a~~)[\(Friedlingstein et al., 2024; Saunio et al., 2025\)](#). CH₄ is the most prevalent non-CO₂ greenhouse gas, with a warming potential 28 times that of CO₂ over 100 years and 84 times over 20 years. (Lee et al., 2023; Montzka et al., 2011; Saunio et al., 2016; Stocker et al., 2013) and an atmospheric lifetime
25 of 9.1 ± 0.9 years (~~Prather et al., 2012~~)[\(Zhou et al., 2023; Saunio et al., 2025\)](#). Starting from 2007, the concentration of CH₄ has proliferated from an annual global mean of 1775 ppb to 1921 ppb in 2024, with a total rise of 146 ppb, which denotes a huge overall growth since the start of ~~industrialisation~~[industrialization](#). The warming of wetlands, an increase in the ruminant population, and a decline in biomass burning—, previously masking the rise in isotopically negative fuel use—, are some of the key factors that may have contributed to the recent surge in CH₄ concentrations (Nisbet et al., 2019). The observed decline
30 in carbon isotope ratio ($\delta^{13}\text{CH}_4$) indicates a shift toward increasing biogenic CH₄ sources, such as microbial emissions from wetlands and agriculture (has a more negative $\delta^{13}\text{CH}_4$ signature) rather than fossil fuel or biomass burning contributions (Skeie et al., 2023; Schaefer et al., 2016). ~~Additionally, the decline of hydroxyl radical (OH), the most dominant CH₄ sink, adds to the total atmospheric CH₄ budget (Stevenson et al., 2020)~~[The long-term trend in OH remains uncertain, with some studies suggesting increases \(e.g. Stevenson et al. \(2020\)\), others finding no significant trend \(Thompson et al., 2024\), and still others showing diverging results depending on methodology \(Saunio et al., 2025\).](#)

The global stock-take under Article 14 of the Paris Agreement implies the responsibility of each party to prepare, communicate, and maintain the successive nationally determined contributions (NDCs) to climate action (EC 2014). A 30 % global reduction in CH₄ emissions from 2020 to 2030 has been aimed at the Global Methane Pledge, launched at a 2021 meeting of the United Nations Framework Convention on Climate Change (UNFCCC). Being one of the significant contributors to
40 greenhouse gas (GHG) emissions, India plays an essential role in the global GHG scenario. Still, it lacks sufficient long-term, continuous, and accurate observations of the GHG to quantify the sources and sinks (Zhang et al., 2014). The country ~~holds high CH₄ emission potential with its largest cattle population,~~[has the largest cattle \(including bovine\) population in the world citeRobinson2014Livestock. Along with this, its huge](#) intense flood irrigation practices, ever-increasing fuel demand, and large wetland extent (nearly 4.7 % of its total geographical area) [contribute to its high CH₄ emission potential](#) (Ganesan et al.,
45 2017; Garg et al., 2011; Ministry of Environment and Change, 2015; Myhre et al., 2013b). CH₄ emissions from enteric fermentation account for about 8 % of the total GHG emissions of India's National GHG inventory 2020 (MoEFCC, 2024). [The](#) Emissions Database for Global Atmospheric Research (EDGAR) inventory provides a global sector-wise emission estimate for CH₄. However, the bottom-up approach of EDGAR inventory is limited by its accuracy and temporal resolution owing to

uncertainties in the data used and methodologies (e.g. uncertain emission factors, aggregation or interpolation errors and sector distribution). Besides, Indian wetland emissions also show inconsistency in estimations (~ 5 to 9%) depending on the wetland model used (Bloom et al., 2017). Janardanan et al. (2024) reported large uncertainty in wetland emission inventory data over the Indian domain based on satellite observations and models. Further, insufficient coverage of highly precise and accurate ground-based observations of CH_4 and inadequate access to emission reporting over the country can lead to misrepresentations in global emission inventories.

Atmospheric concentration measurements contain integrated information on the underlying source-sink distribution. Therefore, integrating atmospheric mixing ratio measurements, flux information from bottom-up approaches, and transport model simulations can potentially enhance CH_4 estimates through inverse modeling (Jones et al., 2021; Cusworth et al., 2022; Bergamaschi et al., 2018) and independently evaluate reported flux estimates. ~~Due to sparse ground data and Previous studies over India have been limited by coarse model resolution, incomplete representation of transport processes, or lack of high-resolution emission inventories. Due to these~~ inadequate modeling systems ~~and sparse ground measurements~~, limited studies have used atmospheric CH_4 observations to inform about CH_4 emission flux estimates across India. There is an ~~imminent-urgent~~ call for measurement that can sufficiently constrain regional emissions in modeling systems (Patra et al., 2016). Recent technological advancements in satellite remote-sensing enable high-resolution-high-density observations to be ~~utilised~~ utilized for this inverse-based quantification when modeling techniques are adequately advanced (Myhre et al., 2013a; Jacob et al., 2016; Alexe et al., 2015; Buchwitz et al., 2017; Liang et al., 2023; Lu et al., 2022). Ganesan et al. (2017) used a top-down approach to estimate India's CH_4 emission for 2010-2015. The above study used column-averaged observations of CH_4 from the Greenhouse Gases Observing Satellite (GOSAT) along with aircraft observations from Civil Aircraft for the Regular Investigation of the Atmosphere Based on an Instrument Container (CARIBIC) and a few surface measurements from Indian sites to calculate methane emissions by atmospheric inverse modeling. Since 2009, GOSAT has measured the atmospheric column for CH_4 every three days at a 10 km diameter circle (Butz et al., 2011). Despite some limitations in temporal coverage, the spatial resolution of GOSAT observations is much better than its predecessor, the Scanning Imaging Absorption Spectrometer for Atmospheric Chartography (SCIAMACHY), which the research community has widely used (Butz et al., 2011; Yokota et al., 2009; Turner et al., 2015; Buchwitz et al., 2005; Schneising et al., 2011).

Since November 2017, the more ~~advanced-recent~~ TROPospheric Monitoring Instrument (TROPOMI) on board the Copernicus Sentinel-5 Precursor satellite provides much higher-density CH_4 observations at a high spatial resolution of $7 \times 7 \text{ km}^2$, upgraded to $5.5 \times 7 \text{ km}^2$ in August 2019 (Hu et al., 2018; Schneising et al., 2023). TROPOMI measures CH_4 at the $2.3 \mu\text{m}$ band, with a swath width of 2600 km (Jacob et al., 2016; Cusworth et al., 2018). These observations are expected to capture

seasonal fluctuations, which, in turn, will give better insight into the source-sink characteristics and quantification. Hence, in the present study, we explore the potential of TROPOMI measurements in representing the distribution of CH₄ fluxes over the Indian region alongside a spatio-seasonal analysis of the CH₄ bottom-up inventory information. We ~~demonstrate the advantage of a modeling system, the Weather Research Forecast~~ use TROPOMI XCH₄ for its dense, near-daily coverage over India, enabling higher comparability with the simulation of 10 km from our Weather Research and Forecasting model coupled with the Chemistry and Greenhouse Gas module (WRF-GHG), ~~operating at a high resolution comparable to TROPOMI, which may minimise~~ which may effectively minimize the forward model-related uncertainties in the carbon assimilation system over India. The performance of this high-resolution model and the advantage of using highly resolved transport fields are previously reported in Thilakan et al. (2022) and Vellalassery et al. (2021). The assessment of the forward model, WRF-GHG, in the atmospheric boundary layer is performed by comparing the atmospheric CH₄ simulations with atmospheric measurements from a ground-based site. Finally, the annual CH₄ emission estimate is also derived for the period 2018-2019 by incorporating the TROPOMI measurements and WRF-GHG forward model in ~~a first-order an~~ atmospheric inversion algorithm. The overview of spatiotemporal analysis of methane-emission patterns across India from global bottom-up inventories, including agriculture, livestock, and fossil-fuel sectors and their impact on column-averaged methane mixing ratio enhancements, provides the context for improving or complementing current emission estimates over India.

The paper is ~~organised~~ organized as follows: Section 2 describes the data and methods used for the study. Section 3 presents data post-processing and inverse analysis, and Section 4 discusses the results of the study ~~from the data analysis conducted~~. The conclusions of the study are presented in Section 5.

2 Data and methods

In this section, we describe the measurements and techniques used for exploring the potential of TROPOMI measurements and the WRF-GHG atmospheric transport model in inferring CH₄ distribution over India. ~~A first-order An~~ inverse method has been devised to deduce the CH₄ fluxes over the Indian region by minimizing mismatches between TROPOMI CH₄ measurements and WRF-GHG mixing ratio simulations, thereby correcting the distribution of prior fluxes. Figure 1 shows the model domain with outlines of each geographical region (more details are given in the subsequent sections) considered in this study.

2.1 TROPOMI observations

The potential of TROPOMI Sentinel-5p to detect significant sources in the ~~single-pass~~ single overpass has been demonstrated in recent publications (Hu et al., 2018; de Gouw et al., 2020; Schneising et al., 2020; Chen et al., 2022; Jacob et al., 2022). We

105 utilized TROPOMI CH₄ observations obtained through the Short Wave Infrared (SWIR) band, centered at approximately 2.3 μm. The atmospheric column-averaged CH₄ mixing ratio (XCH₄) is retrieved using the Weighting Function Modified Differential Optical Absorption Spectroscopy (WFM-DOAS) algorithm. The WFMD algorithm uses a least-squares approach based on scaling prior atmospheric vertical profiles to retrieve XCH₄ and XCO simultaneously (Buchwitz et al., 2007; Schneising et al., 2011). Here, we use the WFMD v1.8 algorithm, for which the efficiency has been validated using Total Carbon Column
110 Observing Network (TCCON) measurements, resulting in an improved random error (12.4 ppb) compared to the previous versions (v1.5 and v1.2) (Schneising et al., 2023). For the analysis, we filtered flagged data and utilized only good-quality retrievals represented by *xch4_quality_flag* = 0.

2.2 Modeling system for atmospheric XCH₄ mixing ratio simulations

We have used the Weather Research and Forecasting model coupled with the Chemistry and Greenhouse Gas module (hereafter
115 referred to as WRF-GHG) for atmospheric CH₄ transport simulations. The core component is the WRF model, based on fully compressible, non-hydrostatic Eulerian equations on terrain-following vertical grids for simulating atmospheric transport (Skamarock et al., 2008). The GHG-TRACER package allows the online passive tracer transport of CH₄ mixing ratio in the atmosphere (Beck, 2011; Pillai et al., 2016). The input fluxes from each emission sector are separately provided as "tagged" tracers when added to the first layer in the modeling system. This allows the decoupling of emission contributions to the total
120 atmospheric CH₄ mixing ratio. We have used the WRF-GHG 3.9.1.1 version with a horizontal resolution of 10 × 10 km² (Lambert conformal conic projection grid) and ~~a~~ an output temporal resolution of 1 hour. The model covers the Indian domain with 307 × 407 grid points and 39 vertical levels. The fifth generation ECMWF reanalysis (ERA-5) data with a horizontal resolution of 0.25° × 0.25° and temporal resolution of 6 hours with 137 vertical levels are used as initial and boundary conditions for meteorology (Hersbach et al. (2020); see Table 1). The model is re-initialized each day with ERA5 meteorology,
125 in which a 6-hour spin-up time was configured. For CH₄ mixing ratio fields, initial and boundary conditions are prescribed from the Copernicus Atmosphere Monitoring Service (CAMS re-analysis data). CAMS provides the simulated atmospheric mixing ratios of CH₄, with a spatial resolution of 0.25° × 0.25° and a temporal resolution of 6 hours on 60 vertical levels (Inness et al. (2019); see Table 1). The model utilizes these initial fields to represent the ~~far-field flux contribution (background~~ ~~) to~~ background of the total mixing ratios. Similar to emission flux contributions, we disentangled the background contribution
130 in the model output to investigate its impacts separately. We have also considered the reported level of uncertainties in CAMS-simulated mixing ratios (e.g. Agustí-Panareda et al. (2023); Wang et al. (2023)) and applied a monthly factor correction (1 to 3 % correction for the whole model domain) to our CAMS-simulated WRF-GHG background to minimize the unrealistic

representation of ~~far-field-background~~ contribution to XCH₄ levels. The corrected WRF-GHG background mixing ratios are hereafter termed simply as background mixing ratios.

135 We used the Emission Database for Global Atmospheric Research (EDGAR v7.0; Crippa et al. (2024)), Global Fire Assimilation System (GFAS v1.2; Kaiser et al. (2012)), and a global wetland CH₄ emissions and uncertainty dataset for atmospheric chemical transport models (WetCHARTs 1.3.1; Bloom et al. (2021)) as prior emission fluxes to represent anthropogenic, biomass burning and wetland emissions respectively. We applied ~~time-temporal scaling~~ factors to the annual EDGAR ~~dataset based on emissions using~~ step-function time profiles (~~Kretschmer et al., 2014~~) ~~and converted it and converted them~~ to 1-hour
140 temporal resolution, ~~following Kretschmer et al. (2014)~~. GFAS data with 0.1° × 0.1° resolution represents biomass burning emissions in the model. GFAS emissions are calculated using fire radiative power observations from the Moderate Resolution Imaging Spectroradiometer (MODIS) instrument aboard the Terra satellite.

WetCHARTs is an ensemble dataset that provides gridded emissions data from 2001 to 2019 at a resolution of 0.50° × 0.50° (Bloom et al., 2017), which were then re-gridded to 0.1° × 0.1° with a temporal resolution of 1 hour. The simulated total
145 atmospheric CH₄ mixing ratio thus contains contributions from the initial fields as well as anthropogenic, biomass burning, and biogenic fields of CH₄. Table 1 summarizes the WRF-GHG model set-up used in this study. The general meteorological configuration for the WRF-GHG model set-up applied here is described in Thilakan et al. (2022).

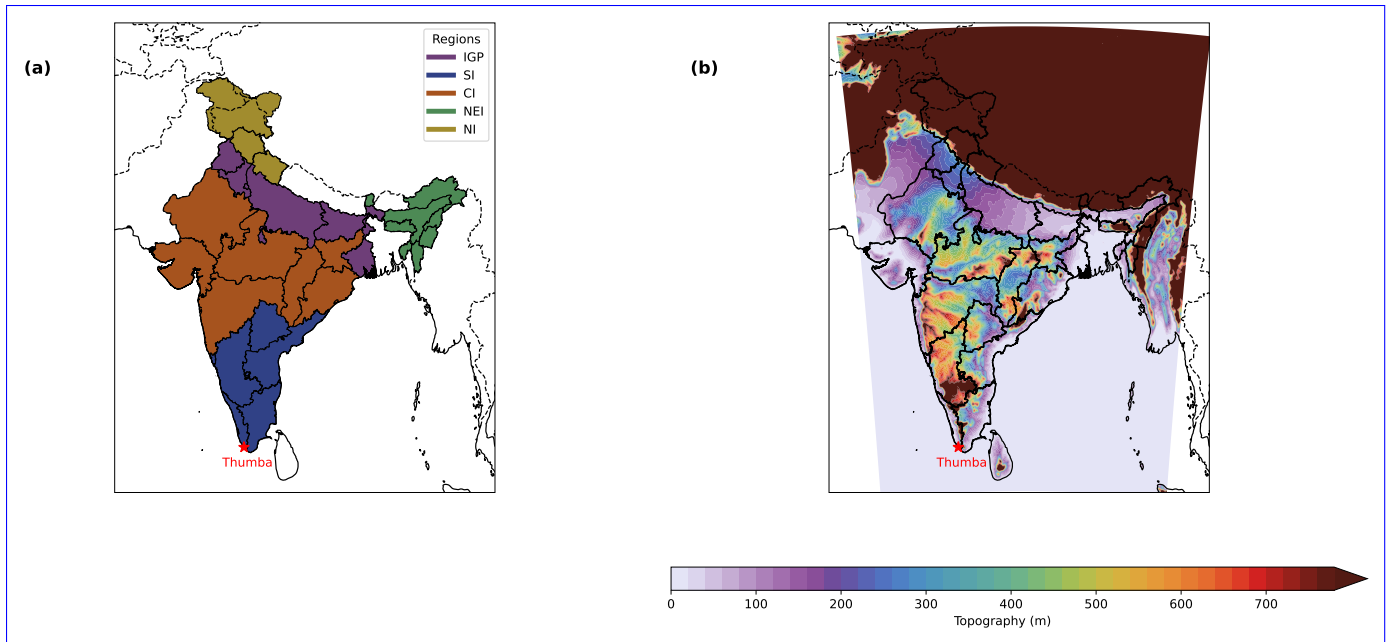


Figure 1. The topographical height contour of the model domain overlaid with outlines of (a) Outlines showing each geographical section region of the Indian landmass according to Survey of India (2024) and (b) the topographical height contour of the model domain. CI stands for Central India, NEI for North East India, NI for North India, SI for South India, and IGP for the Indo Gangetic Plain regions.

| Parameter | Details |
|---|---|
| Domain Configuration | Single domain with a horizontal resolution of 10 km; 39 vertical levels; 307 × 407 grid points |
| Vertical coordinates | Terrain-following hydrostatic pressure vertical coordinates |
| Basic equations | Non-hydrostatic; compressible |
| Grid type | Arakawa C grid |
| Time integration | Third-order Runge–Kutta split explicit |
| Spatial integration | Third- and fifth-order differencing for vertical and horizontal advection, respectively; both for momentum and scalars |
| Time step | 60 s |
| Model top pressure | 50 hPa |
| Physics schemes | Rapid Radiative Transfer Model (RRTM) for longwave and Dudhia for shortwave |
| Radiation | WRF single-moment three-class (WSM3) classic simple ice scheme |
| Microphysics | Yonsei University (YSU) scheme |
| PBL | Monin–Obukhov |
| Surface-layer | NOAH land surface model (LSM) |
| Land-surface | Grell–Freitas ensemble scheme |
| Cumulus | |
| Emission fields | |
| Flux-type | Product Version Spatial res. Temporal res. Source/website Reference |
| Anthropogenic | EDGAR ; Product , Version , Spatial resolution , Temporal resolution ; Reference |
| Biomass-burning | EDGAR ; v7.0 Product , 10 km Annual , 10 km Daily , http://apps.ecmwf.int/datasets/data/cams-gfas/ (Kaiser et al., 2012) (Crippa et al., 2024) |
| Biospheric | WetCHARTs ; v1.2 Product , 10 km Daily , http://apps.ecmwf.int/datasets/data/cams-gfas/ (Kaiser et al., 2012) (Bloom et al., 2017) |
| Initial and lateral boundary conditions | WetCHARTs ; V1.3.1 Product , 0.5 Monthly , Monthly Reference |
| Field | Product , Version , Spatial resolution , Temporal resolution ; Source/website Reference |
| Meteorology | ERA5 NA , 25 km Product , 1 h Reference ; https://cds.climate.copernicus.eu/cdsapp#/home (Hersbach et al., 2020) (Hersbach et al., 2020) |

2.3 Ground-level observations

To assess the model's performance at the surface level, a comparative analysis was conducted using CH₄ *in situ* measurements from a ground-level pollution monitoring station in Thumba (8.5°N, 76.9°E) as denoted in Fig. 1 for 2018 & 2019. Located in southwestern India, Thumba is a tropical coastal station approximately 10 km northwest of Thiruvananthapuram and 500 m inland from the Arabian Sea. This site reflects local to regional influences, but cannot capture the full spatial variability across India. CH₄ concentrations were measured using a greenhouse gas analyzer (model: 911-0011-1001) by Los Gatos Research, USA, based on the off-axis integrated cavity output spectroscopy (OA-ICOS) method (Baer et al., 2002; Raju et al., 2022; Sijikumar et al., 2023; Uma et al., 2024). Air samples were collected from about 10 m above ground level (AGL) using the analyzer's internal pump. Calibration was performed periodically ~~using CH₄ standards supplied by the National Oceanic and Atmospheric Administration (NOAA), USA.~~ However, it should be noted that the instrument can be sensitive to temperature, requiring frequent calibration, which was not regularly met. Measurements were recorded at 1-second intervals, with hourly averages used for subsequent analysis. CH₄ measurement uncertainty is 0.25 % (i.e. 5 ppb with respect to 2000 ppb of CH₄) and the reported precision (1 σ) is 1 ppb.

3 Data post-processing and inverse analysis

2.1 Data post-processing and inverse analysis

We regridded the daily total dry column mixing ratio of CH₄ from TROPOMI at 0.10° × 0.10° resolution, covering a period of 2018 to 2019. From the hourly WRF-GHG CH₄ mixing ratio simulations generated, we sampled those corresponding to the TROPOMI overpass time for the model domain. ~~We~~ The model top is restricted to ~50 hPa (model top pressure), and the model does not take into account stratospheric CH₄ chemistry, which is expected to make a negligible impact on total column averages of CH₄ during the analysis time, considering the methane lifetime in the stratosphere. However, to ensure a fair comparison with observations, we applied the satellite's averaging kernel (AK), as shown in Equation 1, ~~for the model evaluation with observations~~ by considering the vertical sensitivity of the satellite instrument (Schneising et al., 2019). AK is proportional to the sensitivity profile of the measurement that is weighted with the assumed tracer profiles and provides the relation between the retrieved and known tracer profiles. i.e. Applying satellite AK to the model simulations at different vertical levels minimizes the mismatches owing to the instrument vertical sensitivities to the column observations (Eskes and Boersma, 2003; Wang et al., 2023; Schneising, 2024) (Eskes and Boersma, 2003; Wang et al., 2023; Schneising, 2024)

175 We applied the AK to the modeled dry-air CH₄ profiles and derived the dry-air column-averaged mixing ratio of CH₄, Υ_{mod} , as follows:

$$\Upsilon_{\text{mod}} = \sum_l (\Upsilon_{\text{apr}}^l + A_l (\Upsilon_{\text{mod}}^l - \Upsilon_{\text{apr}}^l)) w_l \quad (1)$$

where l is the index of the vertical layer, A_l is the averaging kernel and Υ_{apr}^l is the *a priori* mole fraction of layer l , and Υ_{mod}^l is the corresponding simulated mole fraction of layer l . w_l is the layer-dependent pressure weight.

180 Hence, Υ_{mod} (= XCH_{4,mod}) is used for the model-observation comparisons and inversion analyses. i.e., in this study, Υ_{mod} represents WRF-GHG XCH₄ simulations.

2.2 Estimating optimized CH₄ flux over India

2.1.1 Estimating optimized CH₄ flux over India

We performed a simple Bayesian inverse optimization to deduce the improved emission estimates over the Indian domain. The inversion is designed in such a way that it describes the relationship between the mixing ratio observations and the surface flux emission information (the unknown state) and *a priori* information available. This approach allows us to identify the class of possible states consistent with the available information and to assign a probability density function (pdf) to them. The quantities to be optimized, represented by the state vector \mathbf{x} with n elements $x_1, x_2, x_3, \dots, x_n$ correspond to the ~~total monthly emission information averaged over each political state in India~~ monthly, state-wise emissions from (i) anthropogenic components (EDGAR) and (ii) the sum of anthropogenic (EDGAR) and biomass-burning (GFAS) components, both (i) and (ii) optimized separately. We have omitted the wetland component here since it contributed negligibly to the column-mixing-ratio enhancement. Here, n represents 36 state regions of India. The measured quantities, represented by the measurement vector \mathbf{y} with m elements $y_1, y_2, y_3, \dots, y_m$, represent the total column observations from TROPOMI over a month at $0.1^\circ \times 0.1^\circ$ spatial resolution. Here, m represents the total number of observations available in each political state.

195 The relationship between the measurement vector, \mathbf{y} , and the state vector, \mathbf{x} , can be written as:

$$\mathbf{y} = \mathbf{F}(\mathbf{x}) + \epsilon \quad (2)$$

where $\mathbf{F}(\mathbf{x})$ encapsulates the physics of the measurements as a function of the state vector, described here by our forward ~~transport~~-model, WRF-GHG, which includes forward transport and mapping of flux fields. The error term ϵ includes model error, representation error (sampling mismatch between the observations and the model), and measurement error.

200 Linearizing the forward model to a reference state yields:

$$\mathbf{F}(\mathbf{x}) = \mathbf{K}\mathbf{x} + \epsilon \quad (3)$$

Here, \mathbf{K} is the $m \times n$ Jacobian matrix, representing the sensitivity of the mixing ratio simulated by the forward model to the state vector. The elements of \mathbf{K} are thus: $k_{m,n} = \frac{\partial \mathbf{F}_m(\mathbf{x})}{\partial x_n}$

Since we have not implemented the adjoint model for our forward transport model, the Jacobian was constructed by applying
205 the transport model (WRF-GHG) to ~~the~~ perturbed emissions over the target region (each political state) and obtaining the sensitivity to the corresponding observations, as follows:

$$\mathbf{K} = \frac{(\Upsilon + \Delta \Upsilon) - \Upsilon}{\sum_{\text{TR}} \Phi_{\text{perturbed}} - \sum_{\text{TR}} \Phi} \quad (4)$$

Here, Υ is the column mixing ratio field, and $(\Upsilon + \Delta \Upsilon)$ is the perturbed column mixing ratio field over the target region. Φ is the emission flux field, and $\Phi_{\text{perturbed}}$ is the perturbed emission flux field over the target region (TR).

210 In our implementation, we focus on anthropogenic fluxes and their contributions to the atmospheric dry air column mixing ratios. \mathbf{x}_A represents the prior fluxes, which consist of ~~the spatially averaged~~ monthly anthropogenic (major contributions from enteric fermentation, agricultural soil, waste water handling, and fuel exploitation) and biomass ~~emissions, separately for each political~~ burning emissions. For the optimization, we average the emissions per state. i.e. optimizing one parameter per state representing the total emissions for that state. The ~~far-field~~ background contributions are removed from the observations to
215 optimize the ~~local~~ regional enhancement fluxes. i.e., the measurement vector \mathbf{y} consists of total column observations from TROPOMI subtracted by simulated background mixing ratios over a month at $0.1^\circ \times 0.1^\circ$ spatial resolution.

The background mixing ratios are simulated by WRF-GHG, as explained in Sect. 2.2. We have considered measurement errors (including forward model errors) and prior errors: \mathbf{S}_e and \mathbf{S}_a represent measurement error and prior error covariance matrices, respectively. The measurement error covariance matrix \mathbf{S}_e consists of CH_4 retrieval (\mathbf{y}) and the forward model ($\mathbf{F}(\mathbf{x})$)
220 errors. We assumed a prior emission uncertainty of 80% and a measurement uncertainty of 16 ppb, as adopted from Liang et al. (2023), calculated using the residual error method (Heald et al., 2004). We have not considered cross-correlations; hence,

only the diagonal elements of the ~~matrix~~ matrices \mathbf{S}_e and \mathbf{S}_a are non-zero. The chosen measurement uncertainty encompasses the variability across TROPOMI XCH₄ products (< 16 ppb; see Fig. S1). Nonetheless, as illustrated in Fig. S1, systematic differences exist among XCH₄ products, which are likely to impact the optimization of fine-scale state vectors. Understanding how differences in various retrieval products influence flux estimations is vital for characterizing posterior uncertainty in inverse studies. This necessitates a more sophisticated inverse configuration that also includes a higher discretization of state space and a detailed sensitivity analysis of prior and posterior fluxes across the region, which we consider as a future direction for this study. However, we considered the systematic observational differences due to different retrieval algorithms, as seen in Fig. S1, in a separate inversion by redefining the measurement uncertainty (>50 % more than the originally defined, ~ 25 ppb) that more or less represents the worst case scenario for retrieval differences across the region. The above setup can thus allow us to examine the maximum likelihood impact of such retrieval differences on posterior flux estimates at a national scale.

The solution to the inverse problem is obtained by minimizing the Bayesian scalar cost function $J(\mathbf{x})$ (Rodgers, 2000):

$$J(\mathbf{x}) = (\mathbf{x} - \mathbf{x}_A)^T \mathbf{S}_a^{-1} (\mathbf{x} - \mathbf{x}_A) + (\mathbf{y} - \mathbf{K}\mathbf{x})^T \mathbf{S}_e^{-1} (\mathbf{y} - \mathbf{K}\mathbf{x}_A) \quad (5)$$

where $\nabla_{\mathbf{x}} J(\mathbf{x}) = 0$, the optimal estimate $\hat{\mathbf{x}}$ is obtained (Rodgers, 2000). The state that maximizes the posterior pdf $P(\mathbf{x}|\mathbf{y})$ is the maximum a posteriori solution (MAP). The maximum a posteriori solution is obtained as follows:

$$\hat{\mathbf{x}} = \mathbf{x}_A + \left(\mathbf{K}^T \mathbf{S}_e^{-1} \mathbf{K} + \mathbf{S}_a^{-1} \right)^{-1} \mathbf{K}^T \mathbf{S}_e^{-1} (\mathbf{y} - \mathbf{K}\mathbf{x}_A) \quad (6)$$

Thus, $\hat{\mathbf{x}}$ represents the optimized spatially averaged monthly anthropogenic and biomass burning fluxes corresponding to each political state considered. The posterior error covariance matrix, denoted by $\hat{\mathbf{S}}$, is derived as follows.

$$\hat{\mathbf{S}} = (\mathbf{K}^T \mathbf{S}_e^{-1} \mathbf{K} + \mathbf{S}_a^{-1})^{-1} \quad (7)$$

The error reduction for each month following the inversion procedure (\tilde{e}) is calculated as follows:

$$\tilde{e} = 1 - \frac{\sigma_{post}}{\sigma_{prior}} \quad (8)$$

where σ_{post} is derived as the square root of the diagonal elements of $\hat{\mathbf{S}}$. Similarly, σ_{prior} is obtained from the square root of the diagonal elements of the prior error covariance matrix.

The national budget for annual optimized fluxes \hat{x}_{annual} (in $Tg\ y^{-1}$) is derived as:

$$245 \quad \hat{x}_{annual} = \sum_{t=1}^{N_t} \sum_{s=1}^{N_s} \hat{x}_{s,t}, \quad (9)$$

where $\hat{x}_{s,t}$ represents the estimated value at each political state s for the corresponding month t . N_s is the total number of political states, and N_t is the total number of months considered.

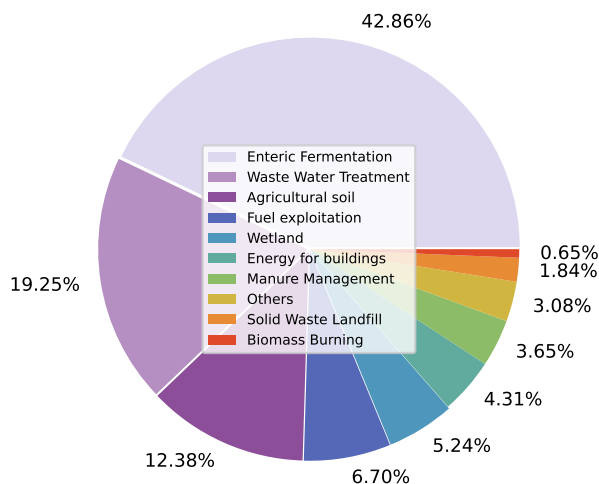
3 Results and Discussion

3.1 Regional and sectoral distribution of CH₄ sources

250 ~~In this section, we present a comparative assessment of different CH₄ sources based on~~ The bottom-up inventories such as EDGAR v8.0 (latest release; Crippa et al. (2024)), WetCHARTs v1.3.1, and GFAS v1.2. ~~Though with inherent uncertainties, these bottom-up inventories relate the~~ relate the GHG emissions to the causative processes by considering ~~the~~ emission activities and emission factors, thereby providing us with a "first guess" to identify the prominent sources (Miller and Michalak, 2017). ~~Major CH₄ emission sources~~, although with inherent uncertainties. In this section, we present a detailed comparative
255 assessment of the sectoral and regional distributions of different CH₄ sources (such as enteric fermentation, wastewater handling, rice agricultural land, wetlands, and biomass burning, ~~are included in detail to assess the sectoral and regional distributions~~).

Our sector-wise analysis of the bottom-up inventories shows that the enteric fermentation associated with the digestive process in cattle makes a significant contribution to CH₄ emissions in India (42.9 %), followed by wastewater treatment (19.2 %),
260 agricultural soil (12.4 %), fuel exploitation (6.7 %), and ~~the~~ wetland (5.2 %, excluding ~~the~~ agriculture) (see Fig.2). The ~~seasonal sources of CH₄~~ sources with significant seasonality include agriculture (see Fig.2 (b)) and biomass burning, also reported in Ganesan et al. (2017). Figure 2. ~~(eS2. (a)-(d))~~ shows an annual average of the spatial distribution of CH₄ emissions for the four major emission sectors in 2018. ~~The positive anthropogenic trend in CH₄~~ Anthropogenic sources are expected to provide the bulk of India's CH₄ emissions in India can be expected owing to the large cattle population and agricultural activities (especially
265 rice production emissions, especially livestock, rice cultivation, and waste management ~~) as indicated by 2010-2015 GOSAT observations~~ (Maasakkers et al., 2019). The annual CH₄ emissions corresponding to rice cultivation (emission from the sector 'Agricultural soil' as given by the EDGAR inventory) show a peak in values over the Indo-Gangetic Plain (IGP) region (Fig.2 eS2 (c)). Several other studies have used GOSAT and other data sources to analyse the CH₄ emissions from rice paddies in India (Miller et al., 2019; Ganesan et al., 2017; Anand et al., 2005). Previous studies reported CH₄ emissions from rice paddies

(a)



(b)

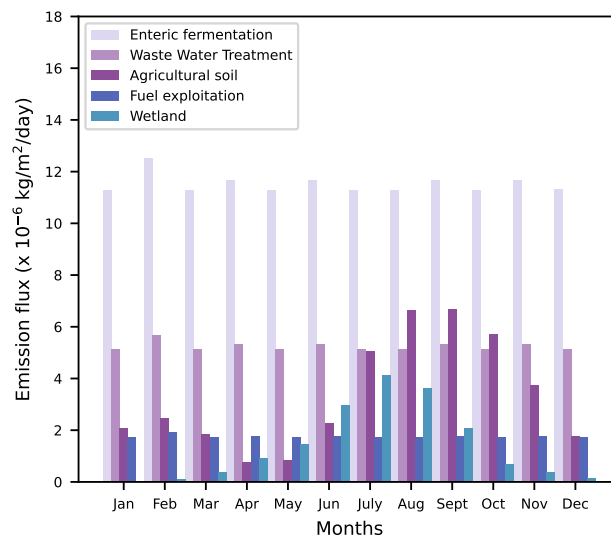


Figure 2. (a) The percentage of contributions of different CH₄ sources towards total annual emission flux over the Indian domain, (b) monthly contribution (calculated from the EDGAR temporal profiles described in Crippa et al. (2020)) from each source, and (c-f) the spatial distribution of the annual CH₄ emission from Enteric fermentation, Waste Water Treatment, Agriculture, and Wetlands, respectively, for 2018.

270 in India of about 3.9 Tg yr⁻¹, with the bulk emitted between June and September (?Garg et al., 2011; Panigrahy et al., 2010) (Janssens-Maenhout et al., 2011; Garg et al., 2011; Panigrahy et al., 2010). The sector-wise analysis of the EDGAR inventory for the year 2018 shows significant CH₄ highs on the eastern coast, including West Bengal and Odisha, which can be attributed to the large rice cultivation in these regions (Crippa et al., 2023). The analysis of monthly emissions from rice cultivation over the year 2018 indicates an increasing pattern in summer monsoon seasons, June to September (see "Agricultural soil" in Fig. 2 275 (b)), with the maximum in August (16.9 %) and September (16.5 %) and the least minimum in April (1.9 %); percentages are shares of the annual flux. There is a smaller peak in February-March time, owing to winter rice cultivation, which comprises 14 % of total rice production in India (Manjunath et al., 2006). Similarly, in the wetland emissions, we also see an increase in monsoon months (Fig. 2 b). The peak wetland emissions are seen in July (24.6 %), followed by August (21.4 %), and the least minimum in January (0.2 %). It has been previously reported from satellite observations that the waterlogged areas increase 280 nearly threefold from the beginning to the end of the monsoon, resulting in increased higher wetland CH₄ emissions (Agarwal and Garg, 2009). The pre-monsoon CH₄ emission (15.5 %) is higher than post-monsoon (6.2 %; see Fig. 2 (b)). This is, possibly due to higher temperatures during the pre-monsoon season as described in Das et al. (2023). Our analysis of monthly emissions based on GFAS shows a peak due to biomass burning in March (65.4 %), with the lowest burning reported in July

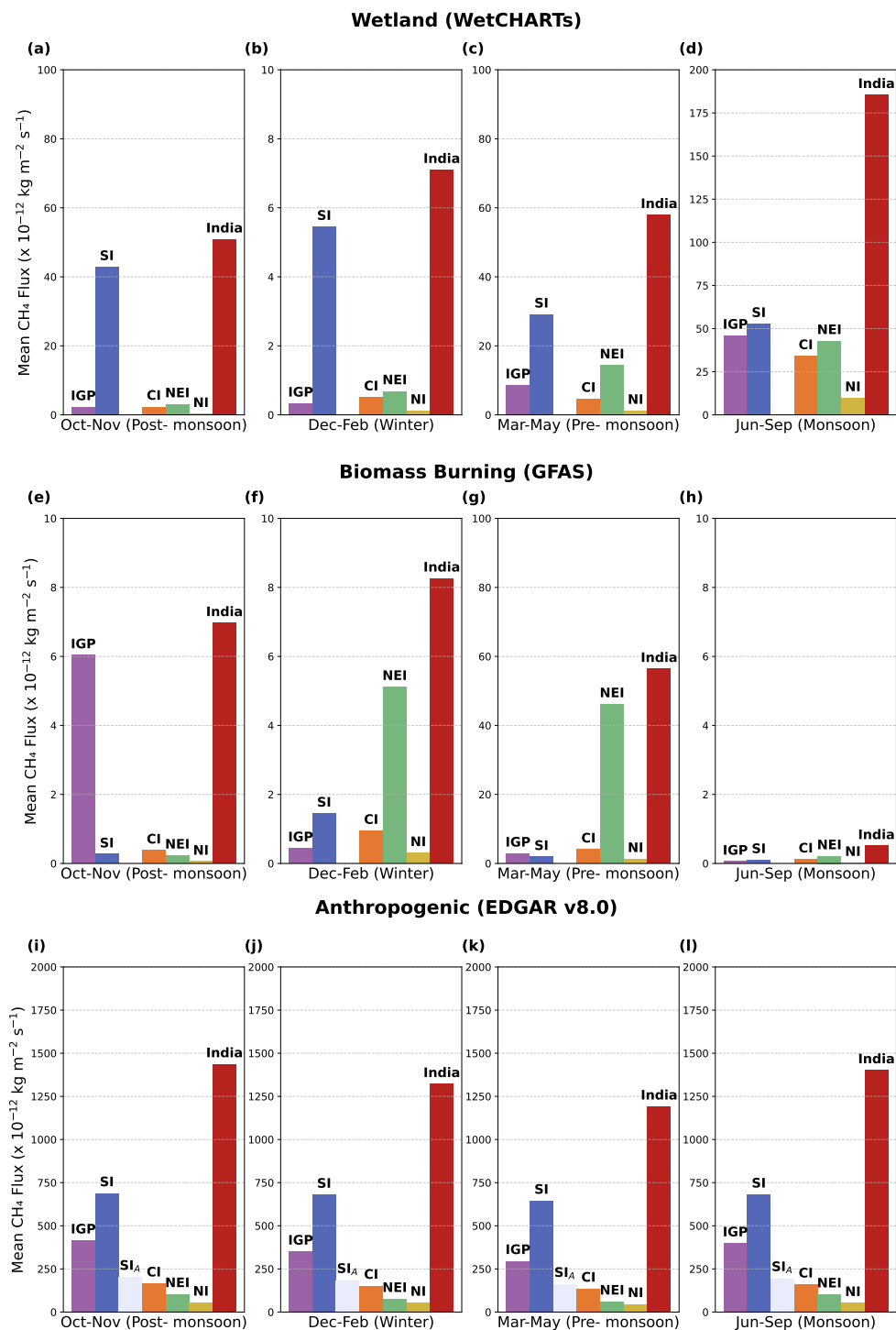


Figure 3. Seasonal mean emissions from (top panels) wetland, (middle panels) biomass burning, and (bottom panels) anthropogenic sources, separated for seasons, for each region as specified in Figure 1. Note: The ranges of the y-axes are not uniform in panels to improve visibility.

(0.1 %) (Fig. 3 (e)-(h)). Other sources of CH₄, including fossil-fuel emissions, enteric fermentation, and wastewater handling, have not shown considerable seasonal variability. A similar pattern has also been observed from the 2019 anthropogenic and natural CH₄ emission analysis (figure not shown).

~~Further, anthropogenic emissions continue to be the most significant contributors to the~~

~~Further, the anthropogenic emissions remain the largest contributors to~~ regional CH₄ emissions (see Fig. 3 & S3). The total anthropogenic emissions (~~sum of various components like enteric fermentation, agriculture soil, wastewater treatment, and fuel exploitation~~), reported by the EDGAR bottom-up inventory (version 8) ~~shows a seasonal peak over the SI, peak seasonally in the South India (SI) region (> 700 × 10⁻¹² kg m⁻² s⁻¹), followed by IGP (> 400 × 10⁻¹² kg m⁻² s⁻¹). The least anthropogenic emissions are seen over NI, which is about a factor of 10 less than that over IGP (, with the minimum emissions observed in North India (NI; see Fig. 3). Generally, the seasonal emission peak is seen in October to November. The peak is typically in October-November, followed by June to September. The emissions are seen at a minimum from March to May. Accordingly, the total June-September, with a minimum in March-May. Total anthropogenic emissions over India (sum of all the given regions as seen in Fig. 3 (i)-(l)) indicate show a peak in October to November October-November and a dip in March-May (ranging from ~1410-1090 1410- 1090 × 10⁻¹² kg m⁻²). While IGP shows consistently high emission distribution spatially high magnitude in spatial distribution (see Fig. 2 (eS2 (a)-(fd)), SI contributes more total emissions than IGP owing to the presence of emissions due to emission hotspots. We have identified four hotspots in SI: Four hotspots identified (see Fig. S5) in SI include one city- Namakkal (11.25 °N, 78.15 °E; in Tamil Nadu), HS1) and three villages- Mandapaka Rural (16.75 °N, 81.65 °E; in Andhra Pradesh HS2), Pasumamla (17.35 °N, 78.65 °E; in Telangana) and Mulkalappalli, HS3), and Mulkalappalli (18.65 °N, 79.55 °E; in Telangana). When those hotspot regions are excluded from SI (labelled as N; HS4). Excluding these hotspots (SI_A), the highest contribution for total emissions is seen over shifts the highest emissions to IGP (see Fig. 3 (i)-(l)). Here, Namakkal in Tamil Nadu has the issue of faces poultry waste deposition (Ramasamy and Manivel, 2019), possibly generating more volatile gases. Mandapaka, as part of the West Godavari district that is known as "Annapurna potentially increasing methane emissions (Ramasamy and Manivel, 2019). Mandapaka in Andhra Pradesh, known as the "(meaning rice bowl) of Andhra Pradesh, has increased rice bowl" of the region, contributes to higher agricultural rice emissions (Gururaj Katti et al., 2002). Pasumamla in Rangareddy district in Telangana has the local poultry industry dumping large amounts of litter in landfills around farms Telangana sees significant poultry waste dumping in landfills (https://rangareddy.telangana.gov.in/animal-husbandry; last accessed: accessed 12 Feb 2025). Mulkappalli is a coal mine location, a coal mining site in Telangana, contributes to the high CH₄ levels in the inventory (https://khammam.telangana.gov.in/economy; last accessed: accessed 12 Feb 2025), contributing~~

to the CH₄ high in the inventory data in SI. Figure S6 shows the methane hotspots over the Indian domain from the coal mining sector as derived from the EDGAR inventory.

Based on WetCHARTs (version 1.3.1), the emissions from natural wetlands are approximated to be natural wetland emissions are approximated at 1.7 Tg yr⁻¹. The regional wetland emissions are high in SI, with peak emissions occurring from June to September ($\sim 185 \times 10^{-12}$ kg m⁻²). The wetland emissions show a peak over the SI region i.e. highest wetland emissions ($>25 \times 10^{-12}$ kg m⁻² s⁻¹ for three seasons) are seen over the SI region in June-September, October-November, and March-May, with a peak emission of $\sim 50 \times 10^{-12}$ kg m⁻² s⁻¹ (see Fig. 3 (a)-(d)). The magnitude is very low for the other regions except for the June to September season. These seasonal peaks can be associated with the possible increased extent of waterlogged areas in monsoon, as discussed previously, with reference to Fig. 2 (b). The biomass Fig. 3). These peaks are likely due to increased waterlogged areas during the monsoon (Fig. 2b). Biomass burning emissions, i.e., those of lesser magnitude compared to total anthropogenic emissions and wetland emissions smaller than wetland and anthropogenic emissions, peak in March-May in most regions except the IGP, generally show a peak in March to May in all regions except for the IGP regions. In the IGP region, the burning of Kharif crop residue where crop residue burning occurs from October to November, as mentioned by Deshpande et al. (2022, 2023), which can also be seen in Fig. 3 (Deshpande et al., 2022, 2023). The maximum seasonal peak is seen in the NEI region during March to May (\sim North East India (NEI) region shows the highest biomass burning emissions in March-May ($\sim 47 \times 10^{-12}$ kg m⁻²), which is about an order higher than that seen over IGP in October-November (see Fig. 3g). This peak in NEI in the March-May season could be due to the extensive slash and burn for clearing weeds preceding the planting season (Deshpande et al., 2023) likely due to slash-and-burn practices before planting (Deshpande et al., 2023). Total emissions (sum of anthropogenic emissions from EDGAR, wetland emissions from WetCHARTs and Biomass Burning emissions from GFAS) follow regional patterns of anthropogenic emissions and peak during combining anthropogenic (EDGAR), wetland (WetCHARTs), and biomass burning (GFAS) emissions, peak in October-November and June-September (Fig. S4 (a) & (d)), with the SI region contributing the highest share at (49.2 % and 46.4 %, respectively. Similarly, SI accounts for the largest contribution in March-May (52 %) and December-February (in March-May and 51.7 %) in December-February.

Though the above estimations give an overview of Indian CH₄ source contributions and their regional patterns, there have been increased concerns about their accuracy due to methodological weaknesses and data gaps (Solazzo et al., 2021; Madrazo et al., 2018). For example, the combined emissions from Oil, Gas, and Coal over the Indian region reported by Scarpelli et al. (2025) is 1.8 Tg yr⁻¹, whereas EDGAR reported 2.2 Tg yr⁻¹. Also, bottom-up methods can overestimate or misinterpret emission sources even at the global level (Saunio et al., 2016). Though inverse modeling can offer better scope in updating improve

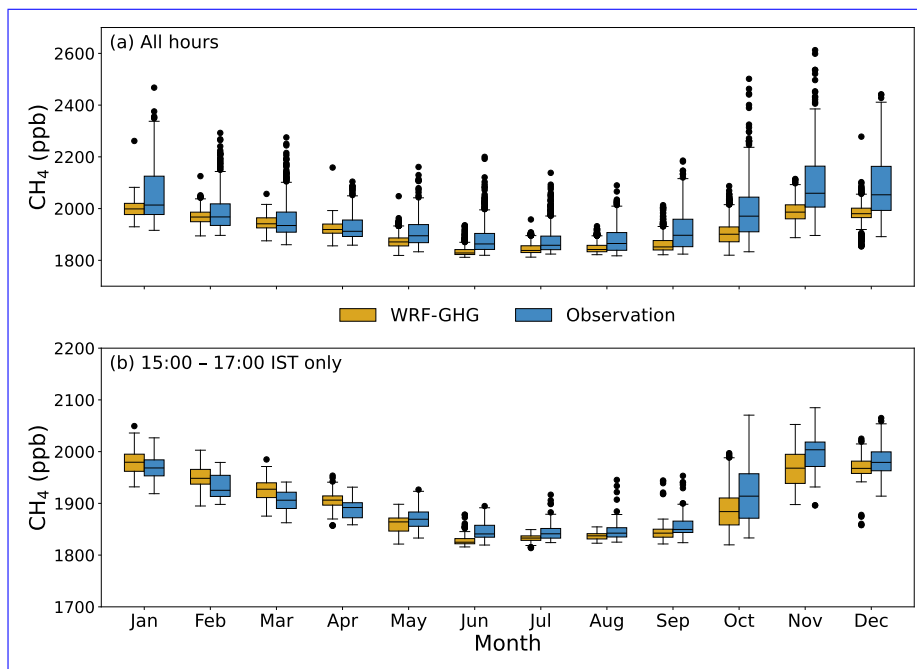


Figure 4. Monthly distribution of observed and WRF-GHG simulated CH₄ mixing ratios at Thumba for 2018 & 2019 for (a) all hours and (b) only 15:00 - 17:00 Local Time (IST hours) (25th and 75th quartiles; see the site location as denoted in Fig. 1). Note that the ranges of the y-axes are not uniform in panels to improve visibility.

the CH₄ budget, those approaches are limited by the significantly, its potential to minimize biases in the bottom-up models used as prior estimates may be limited by insufficient coverage of mixing ratio observations and inadequate representation of the process and spatiotemporal distributions its inadequate representation in the forward models. Satellite instruments such as TROPOMI may aid in high observation density with good spatial coverage (Palmer et al., 2021), the potential of which in the Indian context is explored in further sections.

3.2 Assessment of the forward-model performance against surface measurements

As discussed in Section 2.3, we utilized hourly ground-based observations from a ground-based site, Thumba, to assess the WRF-GHG performance in the planetary boundary layer. The lowest level (approximately 35.2 m) of WRF-GHG-simulated CH₄ at Thumba is compared with surface-level observations of CH₄ and is presented here. Generally, the analysis indicated a reasonable performance of WRF-GHG simulations. CH₄ mixing ratios are found to be lowest during the monsoon season (June–August), increasing from early October and peaking during the post-monsoon and winter months (November–January; see Fig. 4a). The maximum values are seen in December (~ 2100 ppb). The hourly observations show high variability (about 112.7 ppb), but ranging from 1817.4 to 2612.6 ppb for 2018-2019; see Fig. S7. Despite some discrepancies, the WRF-GHG

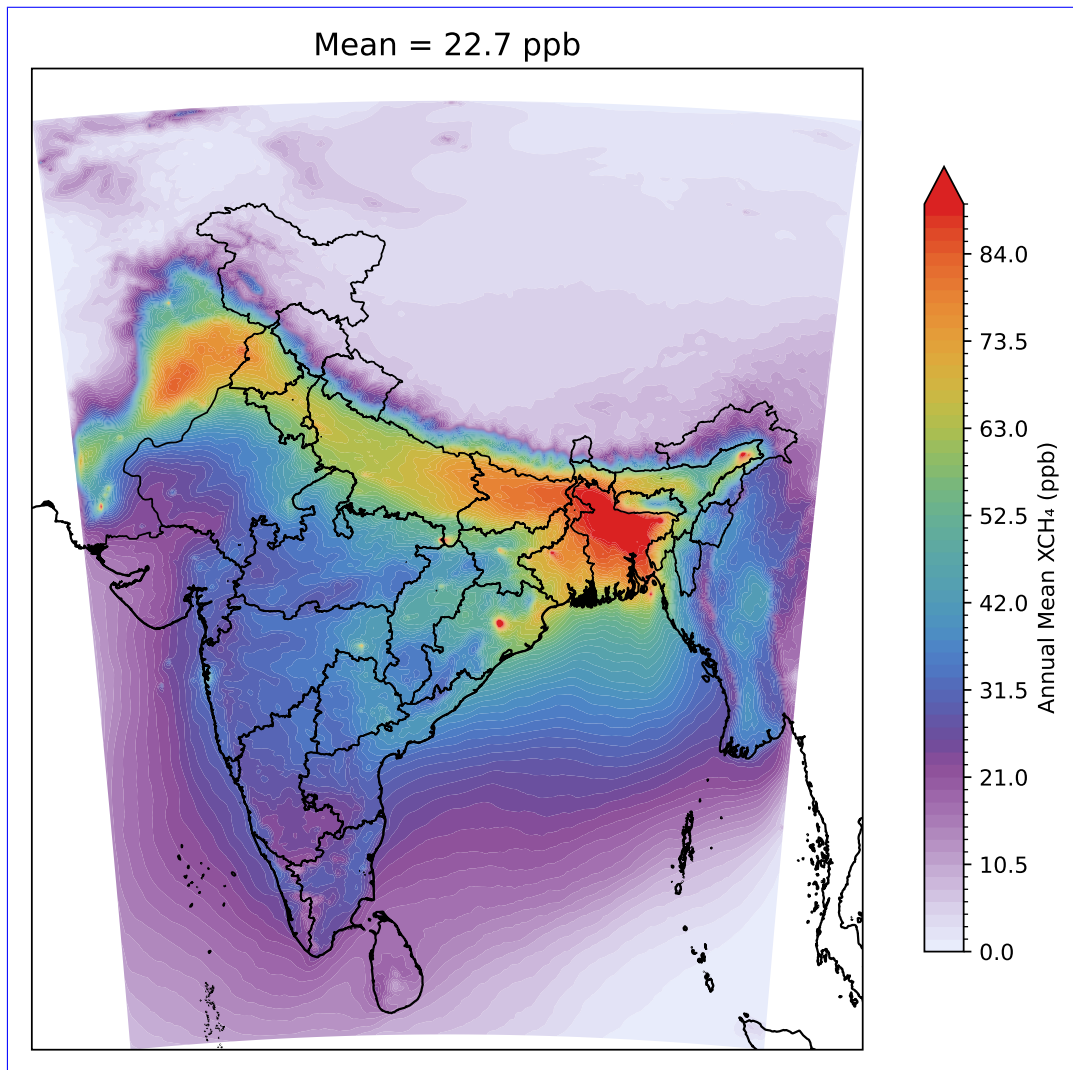


Figure 5. Spatial distribution for annual WRF-GHG simulated anthropogenic mixing ratio enhancement of XCH₄ (including biomass burning) ; separated (a)-(l) for each month of 2018.

simulations broadly align with those highly fluctuating observation patterns, capturing about 56 % of the observed variability.

355 In October, monthly averaged WRF-GHG simulations and TROPOMI observations are strongly correlated, although their absolute values differ substantially (Figure not shown). The mean difference between observations and simulations is 47 ppb, but it shows large model-observation variability of up to 73.9 ppb (Fig. 4(a) and Fig. S7(a)). But, this large discrepancy between the model and observation can be caused by the influence of the fine-scale nocturnal coastal meteorological conditions prevailing in the measurement site as reported in Kavitha et al. (2018). Considering only the afternoon hours, the model-observation

360 differences are reduced to 6.4 ppb, with a maximum difference varying up to 28.1 ppb, capturing about 79 % of observed

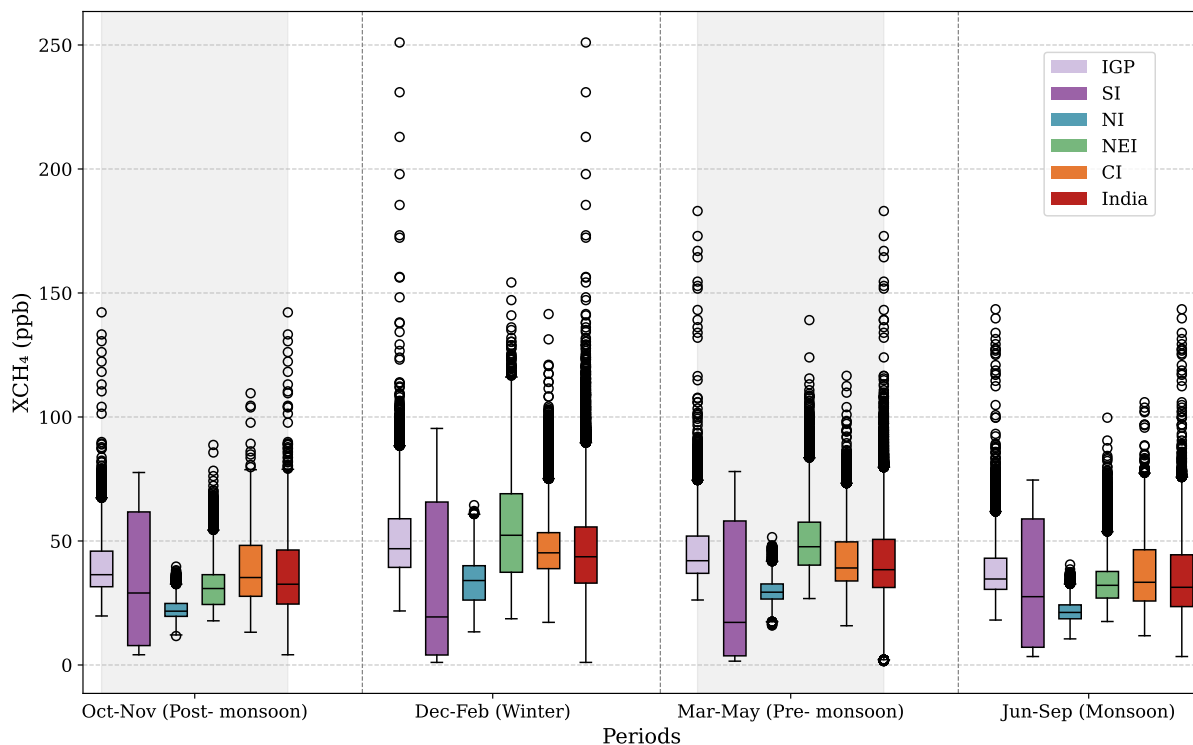


Figure 6. Distribution of seasonal average of simulated mixing ratio enhancement ($XCH_{4,ant} + XCH_{4,bbu}$) over different regions of India in 2018. The box plot displays medians, interquartile ranges, and minimum and maximum values, with data points beyond 1.5 times the interquartile range represented as outliers.

variability (Fig. 4(b) and Fig. S7(b)). The comparison has also been done by removing the boundary contributions from CAMS (see Fig. S8), showing that enhancements correlate ($R^2 = 0.48$) with observed variability. Thus, the above comparison suggests the potential of our model in representing the regional and seasonal variations. The above result is promising, confirming the usability of those afternoon measurements representing well-mixed atmospheric conditions, which can be utilized for future carbon assimilation systems in conjunction with a high-resolution forward modeling framework. As seen for all hours, WRF-GHG generally underestimates surface CH_4 mixing ratios (Fig. S7). Notably, the model-observation differences peaked in winter, owing to the unusually high variability seen in the observations during this period. The effect of enhanced vertical mixing can be seen in the summer months, causing low observed CH_4 magnitude and associated mixing ratio variability. Noteworthy is that the magnitude of observed CH_4 is found to be the smallest during the summer monsoon. While the shallow planetary boundary layer (PBL) in the winter accumulates the effect of surface emissions to the lower boundary, increased boundary layer mixing in the summer can cause lower CH_4 magnitude and variability. Further, Guha et al. (2018) and Metya et al. (2021) report that the influx of clean air from the Southern Hemisphere, carried by the monsoonal south-westerly

winds, can influence the surface CH₄ to lower its concentration. The high rates of OH radical oxidation may also influence surface CH₄ mixing ratios (Lin et al., 2015).

375 Even though WRF-GHG has shown reasonable performance while evaluating the ground-based observations from a complex site (located near the southernmost coastal boundary of the model domain), the robustness of the model needs to be further examined with multiple locations across India when they are available. Those evaluations are particularly necessary for assessing our confidence in the derived posterior fluxes.

3.3 Anthropogenic XCH₄ mixing ratio enhancements

380 In this section, we discuss the mixing ratio enhancements in the atmospheric column in response to spatial and temporal distributions of regional sources for the period 2018-2019. i.e. ~~anthropogenic XCH₄ mixing ratio enhancements consider by~~ considering only contributions from ~~local sources, such as anthropogenic, biomass, and wetland emission sources~~ the sum of anthropogenic and biomass-burning emission sources (mostly human-influenced in India, i.e. from agricultural residue burning and managed fires) over the model domain ~~from the emission inventories, and~~ not using CAMS-derived background XCH₄ ~~(see section 2.2). The IGP and surrounding regions exhibit~~ As mentioned in section 2.4.1, we have also omitted the wetland (biogenic) component here since it contributed negligibly to the column-mixing-ratio enhancement (see Fig. S10). The IGP region exhibits significant XCH₄ enhancements (~~>60 from 27 ppb to 67 ppb~~) from ~~background contribution (far-field fluxes) regional sources~~ attributed to anthropogenic and biomass-burning fluxes (see ~~Fig. S9 Figs. 5~~). Seasonally, ~~compared to summer,~~ the highest XCH₄ enhancements occur during winter (with a maximum of ~ 251 ppb in January); ~~see Fig. S9~~ over India. The 390 minimum enhancement ~~is seen in the monsoon time, possibly due to large-scale mixing in the atmosphere. The increased enhancements in October and November align with additional emissions from agricultural activities such as biomass burning that prevail in some parts of the country. A similar seasonal pattern is also observed in 2019 (see Fig. ??).~~ for the whole Indian domain occurs during the monsoon season (June–September), likely due to a combination of higher boundary layer heights and stronger winds, which enhance vertical and horizontal transport affecting column CH₄ concentrations. The concentrations ~~may also be impacted by the seasonal changes in regional or larger fluxes (>1000 km); however, further investigation is needed to assess their contributions.~~

Figure 6 (also see Fig. S11) shows the regional variability of anthropogenic XCH₄ enhancements across different parts of India as shown in Fig. 1. The highest regional magnitudes and variability in mixing ratio enhancements occur ~~from October to November~~ in the winter season. Here, consistently high magnitude in spatial distribution is found over the IGP region (with 400 a median of ~ ~~55–50~~ ppb), showing maximum values over the SI region (~ ~~100–90~~ ppb) owing to emission hotspots. During

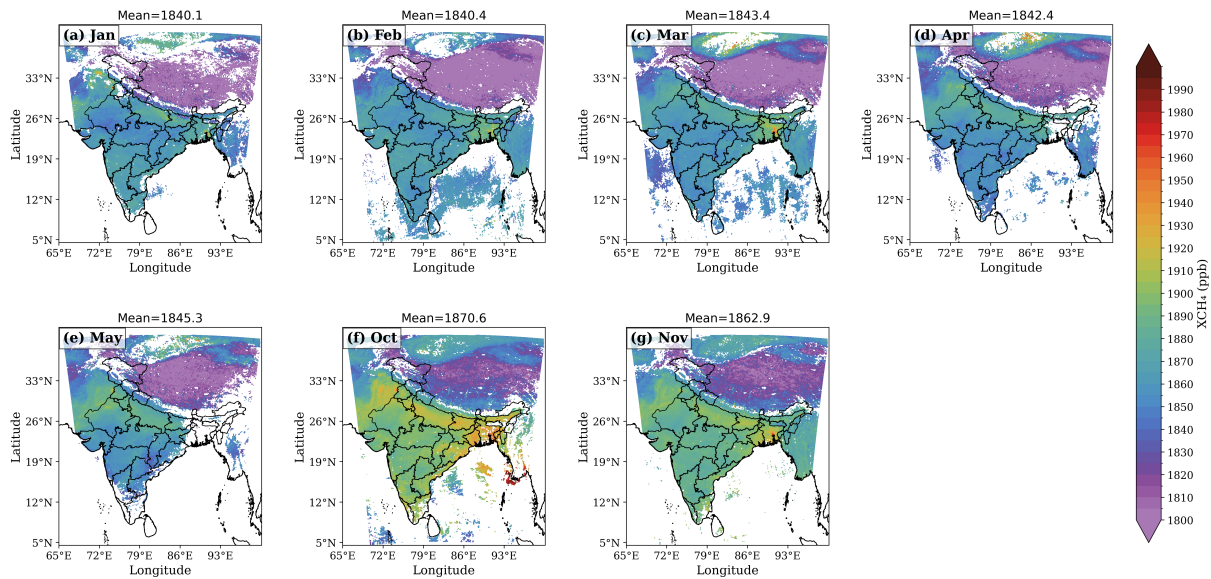


Figure 7. Spatial distribution of the TROPOMI Sentinel-5P measurements, averaged for (a)-(g) each available month in 2018. Some months are excluded due to insufficient data points, due to filtering using the quality flag as given in the data product.

winter, the NEI shows **increased-high** XCH₄ enhancements, with values reaching up to 115 ppb (with a median value of \sim 60 ppb). Winter peaks in XCH₄ likely arise from stable atmospheric transport that carries and concentrates emissions from the preceding October–November period. From June to September, SI enhancements reach up to \sim **95–75** ppb (with a median value of \sim **45–25** ppb). A similar trend is seen for 2019 (Figure not shown). SI exhibits the widest interquartile range with the
 405 lowest minimum value, a relatively low median, and the highest maximum in most seasons, indicating the influence of hotspot emissions, as discussed earlier in Section 4.1.

3.4 Comparison of modeled and observed total XCH₄

In this section, we present our comparisons of WRF-GHG simulations with TROPOMI observations of total XCH₄ in 2018, considering all months in which reasonable amounts of satellite measurements are available after filtering. The details of
 410 filtering are provided in Schneising et al. (2023). TROPOMI observations show distinct seasonal variations in the large spatial domain (Fig. 7), possibly resulting from both atmospheric transport and surface emissions variations. Observations indicate **enhanced-highest** values in the mean spatial distribution of XCH₄ from October to November within the range of \sim 1862 to 1870 ppb. These seasonal increments can be attributed to the shallowing-of-PBL combination of surface emissions, boundary layer height, and horizontal transport, which accumulates the effect of increased-surface emissions the distribution of tracers
 415 at lower atmospheric levels. These increased local emissions, regional emissions, especially from anthropogenic sources, are

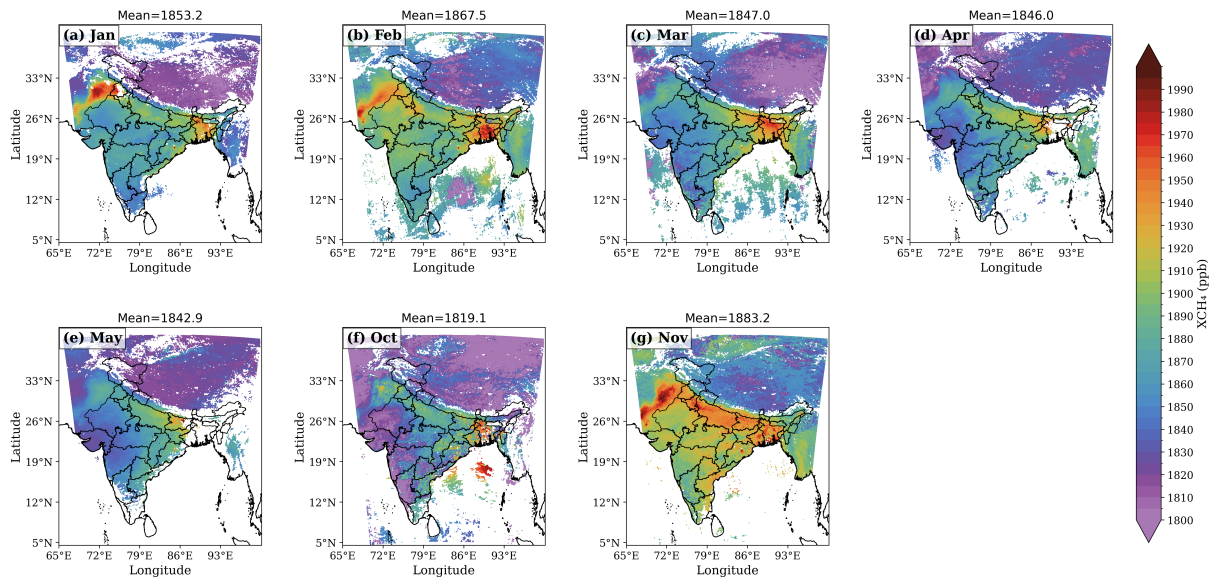


Figure 8. Same as Fig. 7, but showing WRF-GHG simulations of total XCH₄

also seen in Fig. 3, S3 & Fig. 3, which are typical for some parts of India, like the SI and IGP, during the October-November season. However, we cannot neglect the likelihood of increased-bias in the observations due to high aerosol loads, which impacts XCH₄ retrievals (Lorente et al., 2021; Hu et al., 2018; Pandey et al., 2019). All the months show significantly higher total XCH₄ mixing ratios over the IGP region in comparison with the other regions over India. The IGP region is more prone to biomass burning in October and November, causing more aerosols in the region. We have examined the particulate matter (PM_{2.5}) content using the MERRA database, which indicates a heavier aerosol content due to burning during the winter, not always necessarily peaking in October but during the October-February-December-February season (Figure not shown). There is a gradual increase in XCH₄ mixing ratios beginning from the winter month of January till March, with a slight dip in April and then a distinctly high increment in October (exceeding 1870 ppb) in October over the IGP (see Fig. 7. (a)-(f)).

We find that the WRF simulations generally overestimate the total XCH₄ mixing ratio over the Indian region compared to TROPOMI observations, peaking in winter months (maximum at 1883 ppb) (see Fig. 8). The IGP emission hotspot is also pronounced in the EDGAR inventory (Fig. 2S2, see Sect. 4.1), suggesting the increased-large impact of anthropogenic emissions on the observed total XCH₄. Further, the sectoral analysis of the EDGAR emission inventory and the consistency of the spatial pattern with TROPOMI observations indicate that the enhancement over the IGP hotspot can be attributed to anthropogenic emissions from the large cattle population and agricultural activities, especially rice production. Similarly, high XCH₄ values observed along the eastern coast during October and November can be attributed to the wetland-agricultural soil

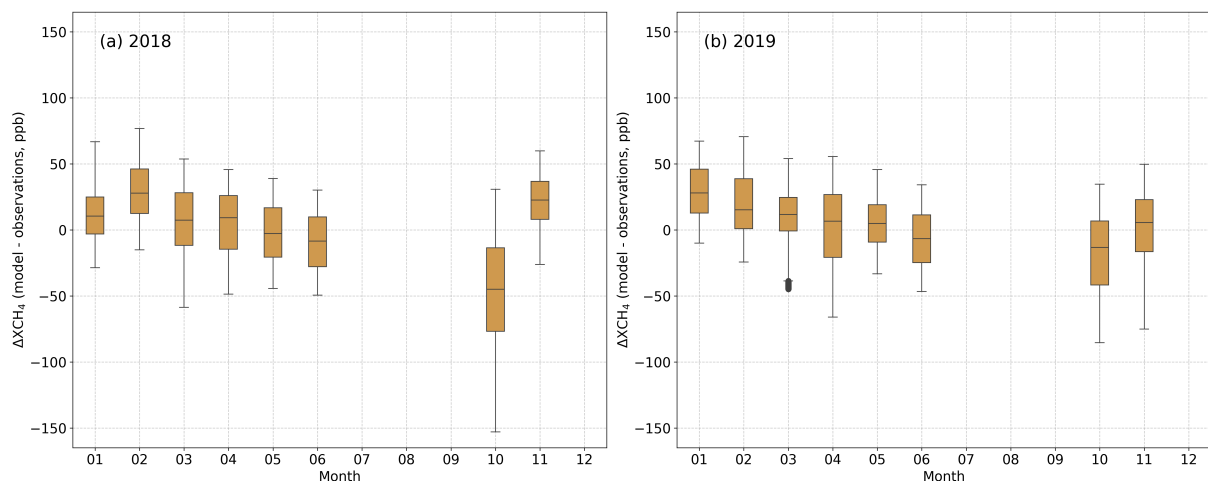


Figure 9. Monthly distribution of the difference between WRF-GHG simulations and TROPOMI Sentinel-5p retrievals of XCH₄ for each available month in 2018 and 2019 when sufficient observations are available (Outliers are not removed; instead, a 90 % winsorization (Wilcox, 2005) is applied for the outliers.)

emissions, as seen in Fig. 2f. [S2c. Wetland emissions also peak on the eastern coast, but the emissions are not found to be high enough to affect the mixing ratio enhancement significantly \(see Fig. S10 & 4\).](#) Table S1 shows the mean observed XCH₄ and the variability over the entire study domain for the non-monsoon months of 2018 and 2019.

435 In general, the WRF-GHG simulations tend to show high bias in the winter months (see Fig. 9). A definite and widespread underestimation by the model was found in October 2018. However, in 2019, WRF-GHG was almost able to capture the observed XCH₄. In the summer months, the model shows patterns of overestimation in eastern India and underestimation in western India. These regional differences in patterns of XCH₄ can arise from heterogeneous sectorial distributions of surface emissions with seasonality that would have been misrepresented in the inventories in conjunction with the large-scale
440 meteorological influences (e.g. southwest monsoon over India, Chandra et al. (2017)).

While the peak total column XCH₄ for TROPOMI falls in October (~ 1870 ppb), that of the WRF-GHG simulations is in November (~ 1883 ppb). However, ~~noteworthy is it is noteworthy~~ that both the model and observation indicate [the](#) XCH₄ peak in either of the [winter](#) months between October and February. The WRF-GHG simulations show a higher variability (standard deviation) than observations for each month. WRF-GHG overestimates the XCH₄ values with a bias of ~~~75~~ [\(72\)](#) [13](#) [\(29\)](#) ppb in
445 2018 (2019)(see Table S1).

3.5 **Assessment of the forward-model performance against surface measurements**

As discussed in Section 2.3, we utilized hourly ground-based observations from a ground-based site, Thumba, to assess the WRF-GHG performance in the planetary boundary layer. The lowest level (approximately 35.2 m) of WRF-GHG-simulated CH₄ at Thumba is compared with surface-level observations of CH₄ and is presented here. Generally, the analysis indicated a reasonable performance of WRF-GHG simulations. CH₄ mixing ratios are found to be lowest during the monsoon season (June–August), increasing from early October and peaking during the post-monsoon and winter months (November–January; see Fig. 4a). The maximum values are seen in December (~ 2100 ppb). The hourly observations show high variability (about 112.7 ppb), but ranging from 1817.4 to 2612.6 ppb for 2018-2019; see Fig. S7. Despite some discrepancies, the WRF-GHG simulations broadly align with those highly fluctuating observation patterns, capturing about 56% of the observed variability. Monthly averaged simulations and observations are found to be highly correlated in October despite their factor of magnitude differences (Figure not shown). The mean difference between observations and simulations is 47 ppb, but it shows large model-observation variability of up to 73.9 ppb (Fig. 4(a) and Fig. S7(a)). But, this large discrepancy between the model and observation can be caused by the influence of the fine-scale nocturnal coastal meteorological conditions prevailing in the measurement site as reported in Kavitha et al. (2018). Considering only the afternoon hours, the model-observation differences are reduced to 6.4 ppb, with a maximum difference varying up to 28.1 ppb, capturing about 79% of observed variability (Fig. 4(b) and Fig. S7(b)). The above result is promising, confirming the usability of those afternoon measurements representing well-mixed atmospheric conditions, which can be utilized for future carbon assimilation systems in conjunction with a high-resolution forward modeling framework. As seen for all hours, WRF-GHG generally underestimates surface CH₄ mixing ratios (Fig. S7). Notably, the model-observation differences peaked in winter, owing to the unusually high variability seen in the observations during this period. The effect of enhanced vertical mixing can be seen in the summer months, causing low observed CH₄ magnitude and associated mixing ratio variability. Noteworthy is that the magnitude of observed CH₄ is found to be the smallest during the summer monsoon. While the shallow planetary boundary layer (PBL) in the winter accumulates the effect of surface emissions to the lower boundary, increased boundary layer mixing in the summer can cause lower CH₄ magnitude and variability. Further, Guha et al. (2018) and Metya et al. (2021) report that the influx of clean air from the Southern Hemisphere, carried by the monsoonal south-westerly winds, can influence the surface CH₄ to lower its concentration. The high rates of OH radical oxidation may also influence surface CH₄ mixing ratios (Lin et al., 2015).

Even though WRF-GHG has shown reasonable performance while evaluating the ground-based observations from a complex site (located near the southernmost coastal boundary of the model domain), the robustness of the model needs to be further examined with multiple locations across India when they are available. Those evaluations are particularly necessary for assessing our confidence in the derived posterior fluxes.

Monthly distribution of observed and WRF-GHG simulated CH₄ mixing ratios at Thumba for 2018 & 2019 for (a) all hours and (b) only 15:00–17:00 Local Time (IST hours) (25th and 75th quartiles; see the site location as denoted in Fig. 1). Note that the ranges of the y-axes are not uniform in panels to improve visibility.

3.5 National CH₄ budget estimation via inverse optimization

480 In this section, we present estimates of India's anthropogenic CH₄ budget for the period 2018-2019, derived through inverse optimization as described in Sect. 3.2. We report posterior emissions separately: one with the impact of biomass burning included and another with biomass burning excluded. The EDGAR emission inventory reports an annual mean CH₄ emission budget of 28.7 Tg yr⁻¹, and we assumed 80% uncertainty (23 Tg yr⁻¹) in our prior as discussed in section 3.1. The posterior annual emission estimate is 24.3 Tg, with the uncertainty reduced to 3.3 Tg. The percentage of error reduction (calculated
485 using Eq. 8) for monthly posterior fluxes ranges from 68 to 92 %. Our inverse model results indicate an overestimation of 14 to 23 % in the EDGAR inventory. Incorporating biomass burning emissions from GFAS has an impact of +0.3 Tg yr⁻¹ on both prior and posterior emission estimates over the Indian region. Although we focus on the national inversion estimates, owing to the inversion approach incorporated, a regional analysis (consistent with Sect. 3.1) of prior and posterior estimates has been presented in Fig. S13 and Fig. S14. As explained in Sect. 2.4.1, we examined the impact of differences in the retrieval
490 algorithm (see Fig. S1), considering the worst-case scenario, on annual posterior flux estimates for the year 2018, showing that the posterior uncertainty increased to 4.4 Tg yr⁻¹ from 3.5 Tg yr⁻¹ at the national scale. Future research is required for fully characterizing the impact of retrieval error uncertainty on posterior flux estimations at a fine scale by employing a more advanced inverse configuration that incorporates higher state space discretization and a detailed sensitivity analysis.

As per the India Fourth Biennial Update Report (BUR4) submitted to the United Nations Framework Convention on Cli-
495 mate Change (UNFCCC) (MoEFCC, 2024), the CH₄ emission budget for India is approximately 19.6 Tg yr⁻¹, which is around 32 % less than the ~~EDGAR-reported~~ EDGAR-reported emissions during the 2018-2019 period. Previous studies also reported an overestimation of the global emission inventories over India. ~~The~~ For instance, Qu et al. (2021) report 41–57 Tg yr⁻¹ anthropogenic CH₄ emission from India, which is significantly higher than our estimations. Also, Zhang et al. (2021) estimate Indian anthropogenic methane emissions of 33±0.6 Tg yr⁻¹, higher than this study estimates. However, the Global Methane
500 Budget ~~2000–2020 (Saunois et al., 2024) reported 21.7 Tg (2000–2017, Saunois et al. (2019))~~, based on top-down approaches using in-situ and GOSAT observations, suggest 25 Tg yr⁻¹ of anthropogenic CH₄ emission from India, but acknowledging large uncertainty ranges in their estimations. Also, bottom-up models' estimates that are compiled in Saunois et al. (2019) and Jackson et al. (2020) indicate a mean anthropogenic CH₄ emission of 21-24 Tg yr⁻¹ from India. The above two estimates align

with our results, though we used independent observations and a different modeling approach. The recent updates on the Global Methane Budget (2000-2020, Saunio et al. (2025)) indicate anthropogenic methane emissions of 37-49 Tg yr⁻¹ for South Asia (including Afghanistan, Bangladesh, Bhutan, India, Nepal, Pakistan, and Sri Lanka), in which around 21.7 Tg yr⁻¹ are contributed from the Indian region (calculated using the data prescribed from Martinez et al. (2024)). Janardanan et al. (2024) reported the annual averaged (2009 - 2020) CH₄ emissions from anthropogenic sectors over the India as 24.2 ± 2.1 Tg yr⁻¹ which is close to our results. The total CH₄ emissions derived from a combination of satellite data (GOSAT), surface and aircraft measurements, and the atmospheric transport model for 2010–2015 were found to be 22 Tg yr⁻¹, which is substantially lower than the emissions reported by the EDGAR v4.2 inventory (Ganesan et al., 2017). ~~Janardanan et al. (2024) reported the annual averaged (2009 - 2020) CH₄ emissions from anthropogenic sectors over the India as 24.2 ± 2.1 Tg yr⁻¹ which is close to our results.~~ On the other hand, Raju et al. (2022) reported that the CH₄ budget for peninsular India is 0.13 Tg yr⁻¹ higher than EDGAR v6.0 inventory-based estimates for the period 2017-2018. These variations in emission reports emphasize the need to improve CH₄ ~~emissions in India~~ emission estimation in India using more regional-specific information and robust methodologies. Our findings also highlight that top-down evaluations of emissions inventories are critical for implementing effective climate change mitigation strategies for countries like India that are largely understudied and undersampled, leading to poor quantification of their contributions in the context of global climate policies.

Although we utilize high-density, high-quality, and high-resolution TROPOMI satellite retrievals together with a high-resolution transport model, our ~~first-order~~ inversion algorithm is limited by its dependence on the spatial distribution of emissions in prior inventories. ~~Prior emission~~ Our optimization adjusts the magnitude of prior emissions over the target region by utilizing additional information from independent measurements, but the present inverse modeling design has the limitation to minimize any flux errors in the spatial distribution, which would have propagated from data sources or bottom-up methodology, cannot be minimized in our optimization procedures sub-scale spatial distribution. However, we expect that those spatial errors may have a minor impact on our annual national estimates owing to our temporal and spatial averaging. ~~Though GFAS inventory includes agricultural residue burning, small fires that are common in smallholders for clearing the wastes and field preparation can be missed from prior inventories, as reported in Deshpande et al. (2022).~~

We excluded natural wetland emissions from the inverse ~~optimisation as we focused on major anthropogenic emission sources. Further, the natural wetland prior emissions~~ optimization as they have resulted in negligible impacts on the column mixing ratio enhancement (~~figure not shown~~ Fig. S10), which is smaller than the uncertainty of the satellite measurement. However, Indian wetland emissions also vary ~~based on~~ among bottom-up inventories and prior models. Approximately 7.5 Tg wetland CH₄ emissions from the Indian region were reported in the Global Methane Budget 2000-2020 (Saunio et al., 2024).

Janardanan et al. (2024) used wetland prior emissions from the Global Methane Budget 2000-2017 (Saunois et al., 2019) in their inversions and reported approximately 3.8 ± 0.16 Tg CH₄ emissions annually from Indian wetlands. At the same time, the BUR4 report (MoEFCC, 2024) has not included the wetland emission estimates, possibly due to inadequate data coverage. Bernard et al. (2025) also discussed the limitations in modeling the wetland emissions from the tropical region due to the inadequacy of available measurements. The above level of estimation discrepancies calls for a country-specific wetland inventory that can also be used as reliable prior fluxes in future inverse modeling. ~~Another limitation can be the~~ Also, there could be a possible overlapping of natural and anthropogenic (agricultural fields) wetlands in the emission inventories used, which may overestimate the sectoral contribution of posterior fluxes (Zhang et al., 2014). Another limitation could be that though the GFAS inventory includes agricultural residue burning, small fires that are common in smallholders for clearing the wastes and field preparation can be missed from prior inventories, as reported in Deshpande et al. (2022). Also, in this study, our focus is restricted to providing national-scale anthropogenic CH₄ emission estimates. While the inversion framework in principle allows for analysis at finer spatial or sectoral scales, here we intentionally report only the aggregated national totals, as our aim is to evaluate the feasibility of TROPOMI–WRF-GHG for constraining India’s methane budget. A more detailed exploration of sectoral and regional signals is left to future work with more coverage of observations and the implementation of more advanced inverse modeling methods.

4 Conclusions

In this study, we investigate the potential of TROPOMI satellite observations along with a high-resolution atmospheric transport model, WRF-GHG, to represent the distribution of CH₄ emissions over the Indian region. Analysis of the bottom-up inventories shows enteric fermentation as the most significant contributor to CH₄ emissions in India (42.9 %), followed by wastewater treatment (19.2 %), agricultural soil (12.4 %), fuel exploitation (6.7 %), and wetlands (5.2 %, excluding agriculture). The above proportions highlight the considerable impact of anthropogenic sources on CH₄ accumulation in the atmosphere. As expected, CH₄ emissions from rice agriculture (August), wetlands (July), and biomass burning (March) exhibit distinct seasonal patterns. The bottom-up anthropogenic CH₄ emissions, and consequently the total atmospheric XCH₄ mixing ratios, have shown some peaks over South India due to a few prominent emission hotspots. This study characterizes regional and seasonal methane-emission patterns from global bottom-up inventories and assesses their possible influence on XCH₄ enhancements. The analysis identifies key uncertainty drivers such as the elevated anthropogenic emissions in the post-monsoon months, thereby guiding refinement of top-down CH₄ estimates across India.

560 The WRF-GHG simulations of XCH₄ mixing ratio enhancements indicate considerable contributions from anthropogenic and biomass burning emissions, particularly in the IGP region (~~>60~~from 27 to 67 ppb). The highest seasonal enhancements of anthropogenic XCH₄ occur during winter, influenced by agricultural emissions, biomass burning, and atmospheric winter transport. This inference aligns with previous studies (eg. Patra et al. (2011)) that shows stronger vertical mixing during the summer, associated with higher boundary layers and faster wind speeds, may impact CH₄ columns. Both the observed and

565 modeled total XCH₄ show significant peaks over the IGP region, with values ranging from ~1862 to ~1870 ppb during October-November. Though WRF-GHG remarkably captures atmospheric XCH₄ patterns, simulations generally overestimate XCH₄ levels compared to TROPOMI. The total XCH₄ along the eastern coast ~~suggests the effects of wetlands on atmospheric column mixing ratios~~reflects the influence of agricultural soil emissions on column-averaged methane. Although wetland emissions peak in this region, their contribution to atmospheric mixing ratios is negligible. Our high-resolution model is

570 capable of capturing surface CH₄ variability, especially for the well-mixed conditions, as confirmed by the ground-based CH₄ observations. However, this comparison is representative of only one station, though it is a complicated measurement location to be represented by the model owing to the influence of coastal meteorology. Such ground-based observations across India are essential for evaluating the full potential of high-resolution models in representing the atmospheric distribution of trace gases and to better constrain vertical transport processes and regional representativeness.

575 The inversion analysis using our high-resolution model and TROPOMI observations reports an annual mean anthropogenic CH₄ emission budget of $24.3 \pm 3.3 \text{ Tg yr}^{-1}$ (excluding biomass burning of 0.3 Tg yr^{-1}). Our estimations are 14 to 23 % lower than the EDGAR emission estimates. At the same time, our estimate is 19 % higher than what the Government of India reported to the UNFCCC for the same period but close to the latest Global Methane Budget 2000-2020 (~~21.7 Tg~~). We emphasize the need for a robust reporting of CH₄ emissions from the Indian region in the global emission inventories, which also require

580 more ground-based atmospheric trace gas measurements along with the advancement of satellite capabilities and atmospheric tracer transport models. With the advancements of denser observational coverage and the high-quality atmospheric transport models, future research can thus explore and evaluate different inverse techniques like ensemble Kalman filter (EnKF) and 4D variational inversion (4D-Var) that can handle highly resolved state vectors, leading to improved emissions at a much finer sub-scale. Overall, the analyses highlight that TROPOMI observations can offer valuable insights into CH₄ emissions, and the

585 WRF-GHG model has the potential to be used in the assimilation system to refine the emissions.

Code and data availability. The anthropogenic CH₄ emission inventories used in this study are downloaded from https://edgar.jrc.ec.europa.eu/archived_datasets (last access: March 2024) (Crippa et al., 2024). CAMS global biomass burning emission based on fire radiative power

(GFAS) is accessed from Copernicus Atmosphere Monitoring Service (CAMS) Atmosphere Data Store, DOI: 10.24381/a05253c7 (last access : November 2023). The global wetland CH₄ emissions, WetCHARTs v1.3.1 is prescribed from <https://daac.ornl.gov/cgi-bin/> (last access: November 2023) (Bloom et al., 2017). The WRF source code is freely available and can be accessed from https://www2.mmm.ucar.edu/wrf/users/download/get_source.html. The TROPOMI/WFMD v1.8 product is made available via https://www.iup.uni-bremen.de/carbon_ghg/products/tropomi_wfmd/.

Author contributions. DP designed the study, TAM and DP performed the model simulations, raw data analysis, and postprocessing, and wrote the initial version of the manuscript. JS, MVD, VT, and AR contributed to the data curation and figures. MB and OS contributed to data archival and processing. SBK contributed to editing. SS, IAG, and SB contributed to the ground-based data collection and pre-processing. All authors contributed to the data analysis, interpretation and writing.

Competing interests. The corresponding author has declared that none of the authors has any competing interests.

Disclaimer. Publisher's note: Copernicus Publications remains neutral with regard to jurisdictional claims made in the text, published maps, institutional affiliations, or any other geographical representation in this paper. While Copernicus Publications makes every effort to include appropriate place names, the final responsibility lies with the authors.

Acknowledgements. This study has been supported by funding from the Indian Ministry of Education and the Max Planck Society in Germany, which has been allocated to IISERB. The University of Bremen team acknowledges funding from ESA via project GHG-CCI+ (ESA contract no. 4000126450/19/I-NB) and the Bundesministerium für Bildung und Forschung within its project ITMS (grant no. 01 LK2103A). We acknowledge the support of IISERB's high-performance cluster system for computations, data analysis, and visualization. The TROPOMI/WFMD retrievals were performed on HPC facilities funded by the Deutsche Forschungsgemeinschaft (grant nos. INST 144/379-1 FUGG and INST 144/493-1 FUGG). This publication contains modified Copernicus Sentinel data (2018–2019). Sentinel-5 Precursor is an ESA mission implemented on behalf of the European Commission. The TROPOMI payload is a joint development by ESA and the Netherlands Space Office (NSO). The Sentinel-5 Precursor ground segment development has been funded by ESA and with national contributions from the Netherlands, Germany, and Belgium. Thara Anna Mathew acknowledges the financial support provided by the Prime Minister's Research [Fellows Fellowship](#) (PMRF) Scheme for providing a fellowship for a PhD. Jithin Sukumaran acknowledges the Council

of Scientific and Industrial Research (CSIR) funding for his PhD fellowship. Imran A Girach acknowledges Prabha R Nair, former scientist at SPL, for supporting the surface trace gas measurements at Thumba utilized in this study. [Special thanks to Navaneetha Jayan and Advait J Vinod for their help with the graphics.](#)

References

- 615 Agarwal, R. and Garg, J.: Methane emission modelling from wetlands and waterlogged areas using MODIS data, *Current Science*, pp. 36–40, 2009.
- Agustí-Panareda, A., Barré, J., Massart, S., Inness, A., Aben, I., Ades, M., Baier, B. C., Balsamo, G., Borsdorff, T., Bousserez, N., Boussetta, S., Buchwitz, M., Cantarello, L., Crevoisier, C., Engelen, R., Eskes, H., Flemming, J., Garrigues, S., Hasekamp, O., Huijnen, V., Jones, L., Kipling, Z., Langerock, B., McNorton, J., Meilhac, N., Noël, S., Parrington, M., Peuch, V.-H., Ramonet, M., Razinger, M., Reuter, M.,
620 Ribas, R., Suttie, M., Sweeney, C., Tarniewicz, J., and Wu, L.: Technical note: The CAMS greenhouse gas reanalysis from 2003 to 2020, *Atmospheric Chemistry and Physics*, 23, 3829–3859, <https://doi.org/https://doi.org/10.5194/acp-23-3829-2023>, 2023.
- Agustí-Panareda, A., Barré, J., Massart, S., Inness, A., Aben, I., Ades, M., Baier, B. C., Balsamo, G., Borsdorff, T., Bousserez, N., et al.: The CAMS greenhouse gas reanalysis from 2003 to 2020, *Atmospheric Chemistry and Physics*, 23, 3829–3859, <https://doi.org/10.5194/acp-23-3829-2023>, 2023.
- 625 Alexe, M., Bergamaschi, P., Segers, A., Detmers, R., Butz, A., Hasekamp, O., Guerlet, S., Parker, R., Boesch, H., Frankenberg, C., et al.: Inverse modelling of CH₄ emissions for 2010–2011 using different satellite retrieval products from GOSAT and SCIAMACHY, *Atmospheric Chemistry and Physics*, 15, 113–133, <https://doi.org/10.5194/acp-15-113-2015>, 2015.
- Anand, S., Dahiya, R., Talyan, V., and Vrat, P.: Investigations of methane emissions from rice cultivation in Indian context, *Environment International*, 31, 469–482, <https://doi.org/10.1016/j.envint.2004.10.016>, 2005.
- 630 Baer, D. S., Paul, J. B., Gupta, M., and O’keefe, A.: Sensitive absorption measurements in the near-infrared region using off-axis integrated-cavity-output spectroscopy, *Applied Physics B*, 75, 261–265, <https://doi.org/10.1007/s00340-002-0971-z>, 2002.
- Beck, V.: *The WRF Greenhouse Gas Model (WRF-GHG)*, 2011.
- Bergamaschi, P., Karstens, U., Manning, A. J., Saunio, M., Tsuruta, A., Berchet, A., Vermeulen, A. T., Arnold, T., Janssens-Maenhout, G., Hammer, S., et al.: Inverse modelling of European CH₄ emissions during 2006–2012 using different inverse models and reassessed
635 atmospheric observations, *Atmospheric Chemistry and Physics*, 18, 901–920, <https://doi.org/https://doi.org/10.5194/acp-18-901-2018>, 2018.
- Bernard, J., Salmon, E., Saunio, M., Peng, S., Serrano-Ortiz, P., Berchet, A., Gnanamoorthy, P., Jansen, J., and Ciais, P.: Satellite-based modeling of wetland methane emissions on a global scale (SatWetCH₄ 1.0), *Geoscientific Model Development*, 18, 863–883, <https://doi.org/10.5194/egusphere-2024-1331>, 2025.
- 640 Bloom, A., Bowman, K., Lee, M., Turner, A., Schroeder, R., Worden, J., Weidner, R., McDonald, K., and Jacob, D.: CMS: global 0.5-deg wetland methane emissions and uncertainty (WetCHARTs v1. 3.1), ORNL DAAC, <https://doi.org/10.3334/ORNLDAAAC/1915>, 2021.
- Bloom, A. A., Bowman, K. W., Lee, M., Turner, A. J., Schroeder, R., Worden, J. R., Weidner, R., McDonald, K. C., and Jacob, D. J.: A global wetland methane emissions and uncertainty dataset for atmospheric chemical transport models (WetCHARTs version 1.0), *Geoscientific Model Development*, 10, 2141–2156, <https://doi.org/10.5194/gmd-10-2141-2017>, 2017.

- 645 Buchwitz, M., Khlystova, I., Bovensmann, H., and Burrows, J.: Three years of global carbon monoxide from SCIAMACHY: comparison with MOPITT and first results related to the detection of enhanced CO over cities, *Atmospheric Chemistry and Physics*, 7, 2399–2411, <https://doi.org/10.5194/acp-7-2399-2007>, 2007.
- Buchwitz, M., Schneising, O., Reuter, M., Heymann, J., Krautwurst, S., Bovensmann, H., Burrows, J. P., Boesch, H., Parker, R. J., Somkuti, P., et al.: Satellite-derived methane hotspot emission estimates using a fast data-driven method, *Atmospheric Chemistry and Physics*, 17, 5751–5774, <https://doi.org/10.5194/acp-17-5751-2017>, 2017.
- 650 Buchwitz, M. d., De Beek, R., Burrows, J., Bovensmann, H., Warneke, T., Notholt, J., Meirink, J., Goede, A., Bergamaschi, P., Körner, S., et al.: Atmospheric methane and carbon dioxide from SCIAMACHY satellite data: initial comparison with chemistry and transport models, *Atmospheric Chemistry and Physics*, 5, 941–962, <https://doi.org/https://doi.org/10.5194/acp-5-941-2005>, 2005.
- Butz, A., Guerlet, S., Hasekamp, O., Schepers, D., Galli, A., Aben, I., Frankenberg, C., Hartmann, J.-M., Tran, H., Kuze, A., et al.: Toward accurate CO₂ and CH₄ observations from GOSAT, *Geophysical Research Letters*, 38, <https://doi.org/10.1029/2011GL047888>, 2011.
- 655 Chandra, N., Hayashida, S., Saeki, T., and Patra, P. K.: What controls the seasonal cycle of columnar methane observed by GOSAT over different regions in India?, *Atmospheric Chemistry and Physics*, 17, 12 633–12 643, <https://doi.org/10.5194/acp-17-12633-2017>, 2017.
- Chen, Z., Jacob, D. J., Nesser, H., Sulprizio, M. P., Lorente, A., Varon, D. J., Lu, X., Shen, L., Qu, Z., Penn, E., et al.: Methane emissions from China: a high-resolution inversion of TROPOMI satellite observations, *Atmospheric Chemistry and Physics*, 22, 10 809–10 826, <https://doi.org/10.5194/acp-22-10809-2022>, 2022.
- 660 Ciais, P., Sabine, C., Bala, G., Bopp, L., Brovkin, V., House, J. I., et al.: Carbon and other biogeochemical cycles, in: *Climate Change 2013: The Physical Science Basis. Contribution of Working Group I to the Fifth Assessment Report of the Intergovernmental Panel on Climate Change*, pp. 465–570, Cambridge University Press, <https://doi.org/10.1017/CBO9781107415324.015>, 2014.
- Crippa, M., Solazzo, E., Huang, G., Guizzardi, D., Koffi, E., Muntean, M., Schieberle, C., Friedrich, R., and Janssens-Maenhout, G.: High resolution temporal profiles in the Emissions Database for Global Atmospheric Research, *Scientific data*, 7, 121, <https://doi.org/10.6084/m9.figshare.12052887>, 2020.
- 665 Crippa, M., Guizzardi, D., Pagani, F., Schiavina, M., Melchiorri, M., Pisoni, E., Graziosi, F., Muntean, M., Maes, J., Dijkstra, L., et al.: Insights on the spatial distribution of global, national and sub-national GHG emissions in edgarv8. 0, *Earth System Science Data Discussions*, 2023, 1–28, <https://doi.org/https://doi.org/10.5194/essd-16-2811-2024>, 2023.
- 670 Crippa, M., Guizzardi, D., Pagani, F., Schiavina, M., Melchiorri, M., Pisoni, E., Graziosi, F., Muntean, M., Maes, J., Dijkstra, L., et al.: Insights into the spatial distribution of global, national, and subnational greenhouse gas emissions in the Emissions Database for Global Atmospheric Research (EDGAR v8. 0), *Earth System Science Data*, 16, 2811–2830, <https://doi.org/10.5194/essd-16-2811-2024>, 2024.
- Cusworth, D. H., Jacob, D. J., Sheng, J.-X., Benmergui, J., Turner, A. J., Brandman, J., White, L., and Randles, C. A.: Detecting high-emitting methane sources in oil/gas fields using satellite observations, *Atmospheric Chemistry and Physics*, 18, 16 885–16 896, <https://doi.org/10.5194/acp-18-16885-2018>, 2018.
- 675

- Cusworth, D. H., Thorpe, A. K., Ayasse, A. K., Stepp, D., Heckler, J., Asner, G. P., Miller, C. E., Yadav, V., Chapman, J. W., Eastwood, M. L., et al.: Strong methane point sources contribute a disproportionate fraction of total emissions across multiple basins in the United States, *Proceedings of the National Academy of Sciences*, 119, e2202338 119, <https://doi.org/10.1073/pnas.2202338119>, 2022.
- 680 Das, N., Chakraborty, R., Pal, S. C., Mondal, A., and Mandal, S.: A novel coupled framework for detecting hotspots of methane emission from the vulnerable Indian Sundarban mangrove ecosystem using data-driven models, *Science of The Total Environment*, 866, 161 319, <https://doi.org/10.1016/j.scitotenv.2022.161319>, 2023.
- de Gouw, J., Veefkind, J., Roosenbrand, E., Dix, B., Lin, J., Landgraf, J., and Levelt, P.: Daily Satellite Observations of Methane from Oil and Gas Production Regions in the United States, *Scientific Reports*, 10, <https://doi.org/10.1038/s41598-020-57678-4>, 2020.
- Deshpande, M. V., Pillai, D., and Jain, M.: Detecting and quantifying residue burning in smallholder systems: An integrated approach using Sentinel-2 data, *International Journal of Applied Earth Observation and Geoinformation*, 108, 102 761, <https://doi.org/10.1016/j.jag.2022.102761>, 2022.
- 685 Deshpande, M. V., Kumar, N., Pillai, D., Krishna, V. V., and Jain, M.: Greenhouse gas emissions from agricultural residue burning have increased by 75% since 2011 across India, *Science of the Total Environment*, 904, 166 944, <https://doi.org/10.1016/j.scitotenv.2023.166944>, 2023.
- 690 Eskes, H. and Boersma, K.: Averaging kernels for DOAS total-column satellite retrievals, *Atmospheric Chemistry and Physics*, 3, 1285–1291, <https://doi.org/10.5194/acp-3-1285-2003>, 2003.
- Friedlingstein, P., O'sullivan, M., Jones, M. W., Andrew, R. M., Hauck, J., Landschützer, P., Le Quéré, C., Li, H., Luijkx, I. T., Olsen, A., et al.: Global carbon budget 2024, *Earth System Science Data Discussions*, 2024, 1–133, 2024.
- Ganesan, A. L., Rigby, M., Lunt, M. F., Parker, R. J., Boesch, H., Goulding, N., Umezawa, T., Zahn, A., Chatterjee, A., Prinn, R. G., et al.: Atmospheric observations show accurate reporting and little growth in India's methane emissions, *Nature Communications*, 8, 836, <https://doi.org/DOI: 10.1038/s41467-017-00994-7>, 2017.
- 695 Garg, A., Kankal, B., and Shukla, P.: Methane emissions in India: Sub-regional and sectoral trends, *Atmospheric environment*, 45, 4922–4929, <https://doi.org/10.1016/j.atmosenv.2011.06.004>, 2011.
- Guha, T., Tiwari, Y. K., Valsala, V., Lin, X., Ramonet, M., Mahajan, A., Datye, A., and Kumar, K. R.: What controls the atmospheric methane seasonal variability over India?, *Atmospheric Environment*, 175, 83–91, <https://doi.org/10.1016/j.atmosenv.2017.11.042>, 2018.
- 700 Gururaj Katti, G. K., Pasalu, I., Rao, P., Varma, N., and Krishnaiah, K.: Farmer's participatory approach to improve pest management decision making in high production systems of rice in Andhra Pradesh-a case study., <https://doi.org/DOI: 10.1080/14735903.2022.2070340>, 2002.
- Heald, C. L., Jacob, D. J., Jones, D. B., Palmer, P. I., Logan, J. A., Streets, D., Sachse, G. W., Gille, J. C., Hoffman, R. N., and Nehr Korn, T.: Comparative inverse analysis of satellite (MOPITT) and aircraft (TRACE-P) observations to estimate Asian sources of carbon monoxide, *Journal of Geophysical Research: Atmospheres*, 109, <https://doi.org/10.1029/2004JD005185>, 2004.
- 705

- Hersbach, H., Bell, B., Berrisford, P., Hirahara, S., Horányi, A., Muñoz-Sabater, J., Nicolas, J., Peubey, C., Radu, R., Schepers, D., et al.: The ERA5 global reanalysis, *Quarterly Journal of the Royal Meteorological Society*, 146, 1999–2049, <https://doi.org/https://doi.org/10.1002/qj.3803>, 2020.
- 710 Hu, H., Landgraf, J., Detmers, R., Borsdorff, T., Aan de Brugh, J., Aben, I., Butz, A., and Hasekamp, O.: Toward global mapping of methane with TROPOMI: First results and intersatellite comparison to GOSAT, *Geophysical Research Letters*, 45, 3682–3689, <https://doi.org/https://doi.org/10.1002/2018GL077259>, 2018.
- Inness, A., Ades, M., Agustí-Panareda, A., Barré, J., Benedictow, A., Blechschmidt, A.-M., Dominguez, J. J., Engelen, R., Eskes, H., Fleming, J., et al.: The CAMS reanalysis of atmospheric composition, *Atmospheric Chemistry and Physics*, 19, 3515–3556, 2019.
- Jackson, R. B., Saunio, M., Bousquet, P., Canadell, J. G., Poulter, B., Stavert, A. R., Bergamaschi, P., Niwa, Y., Segers, A., and Tsuruta, A.: 715 Increasing anthropogenic methane emissions arise equally from agricultural and fossil fuel sources, *Environmental Research Letters*, 15, 071 002, <https://doi.org/10.1088/1748-9326/ab9ed2>, 2020.
- Jacob, D. J., Turner, A. J., Maasackers, J. D., Sheng, J., Sun, K., Liu, X., Chance, K., Aben, I., McKeever, J., and Frankenberg, C.: Satellite observations of atmospheric methane and their value for quantifying methane emissions, *Atmospheric Chemistry and Physics*, 16, 14 371–14 396, <https://doi.org/10.5194/acp-16-14371-2016>, 2016.
- 720 Jacob, D. J., Varon, D. J., Cusworth, D. H., Dennison, P. E., Frankenberg, C., Gautam, R., Guanter, L., Kelley, J., McKeever, J., Ott, L. E., et al.: Quantifying methane emissions from the global scale down to point sources using satellite observations of atmospheric methane, *Atmospheric Chemistry and Physics*, 22, 9617–9646, <https://doi.org/10.5194/acp-22-9617-2022>, 2022.
- Janardanan, R., Maksyutov, S., Wang, F., Nayagam, L., Sahu, S. K., Mangaraj, P., Saunio, M., Lan, X., and Matsunaga, T.: Country-level methane emissions and their sectoral trends during 2009–2020 estimated by high-resolution inversion of GOSAT and surface observations, 725 *Environmental Research Letters*, 19, 034 007, <https://doi.org/DOI 10.1088/1748-9326/ad2436>, 2024.
- Janssens-Maenhout, G., Crippa, M., Guizzardi, D., Muntean, M., and Schaaf, E.: Emissions Database for Global Atmospheric Research (EDGAR), version v4.2 (time-series), <http://data.europa.eu/89h/jrc-edgar-emissiontimeseriesv42>, 2011.
- Jones, T. S., Franklin, J. E., Chen, J., Dietrich, F., Hajny, K. D., Paetzold, J. C., Wenzel, A., Gatley, C., Gottlieb, E., Parker, H., et al.: Assessing urban methane emissions using column-observing portable Fourier transform infrared (FTIR) spectrometers and a novel Bayesian 730 inversion framework, *Atmospheric Chemistry and Physics*, 21, 13 131–13 147, <https://doi.org/https://doi.org/10.5194/acp-21-13131-2021>, 2021.
- Kaiser, J., Heil, A., Andreae, M., Benedetti, A., Chubarova, N., Jones, L., Morcrette, J.-J., Razinger, M., Schultz, M., Suttie, M., et al.: Biomass burning emissions estimated with a global fire assimilation system based on observed fire radiative power, *Biogeosciences*, 9, 527–554, <https://doi.org/10.5194/bg-9-527-2012>, 2012.
- 735 Kavitha, M., Nair, P. R., Girach, I., Aneesh, S., Sijikumar, S., and Renju, R.: Diurnal and seasonal variations in surface methane at a tropical coastal station: Role of mesoscale meteorology, *Science of The Total Environment*, 631–632, 1472–1485, <https://doi.org/10.1016/j.scitotenv.2018.03.123>, 2018.

- Kretschmer, R., Gerbig, C., Karstens, U., Biavati, G., Vermeulen, A., Vogel, F., Hammer, S., and Totsche, K.: Impact of optimized mixing heights on simulated regional atmospheric transport of CO₂, *Atmospheric Chemistry and Physics*, 14, 7149–7172, <https://doi.org/10.5194/acp-14-7149-2014>, 2014.
- 740 Lee, H., Calvin, K., Dasgupta, D., Krinner, G., Mukherji, A., Thorne, P., Trisos, C., Romero, J., Aldunce, P., Barret, K., et al.: IPCC, 2023: Climate Change 2023: Synthesis Report, Summary for Policymakers. Contribution of Working Groups I, II and III to the Sixth Assessment Report of the Intergovernmental Panel on Climate Change [Core Writing Team, H. Lee and J. Romero (eds.)]. IPCC, Geneva, Switzerland., 2023.
- 745 Liang, R., Zhang, Y., Chen, W., Zhang, P., Liu, J., Chen, C., Mao, H., Shen, G., Qu, Z., Chen, Z., et al.: East Asian methane emissions inferred from high-resolution inversions of GOSAT and TROPOMI observations: a comparative and evaluative analysis, *Atmospheric Chemistry and Physics*, 23, 8039–8057, <https://doi.org/10.5194/acp-23-8039-2023>, 2023.
- Lin, X., Indira, N., Ramonet, M., Delmotte, M., Ciais, P., Bhatt, B., Reddy, M., Angchuk, D., Balakrishnan, S., Jorphail, S., et al.: Long-lived atmospheric trace gases measurements in flask samples from three stations in India, *Atmospheric Chemistry and Physics*, 15, 9819–9849, <https://doi.org/10.5194/acp-15-9819-2015>, 2015.
- 750 Lorente, A., Borsdorff, T., Butz, A., Hasekamp, O., Schneider, A., Wu, L., Hase, F., Kivi, R., Wunch, D., Pollard, D. F., et al.: Methane retrieved from TROPOMI: improvement of the data product and validation of the first 2 years of measurements, *Atmospheric Measurement Techniques*, 14, 665–684, <https://doi.org/10.5194/amt-14-665-2021>, 2021.
- Lu, X., Jacob, D. J., Wang, H., Maasackers, J. D., Zhang, Y., Scarpelli, T. R., Shen, L., Qu, Z., Sulprizio, M. P., Nesser, H., et al.: Methane emissions in the United States, Canada, and Mexico: evaluation of national methane emission inventories and 2010–2017 sectoral trends by inverse analysis of in situ (GLOBALVIEWplus CH₄ ObsPack) and satellite (GOSAT) atmospheric observations, *Atmospheric Chemistry and Physics*, 22, 395–418, <https://doi.org/https://doi.org/10.5194/acp-22-395-2022>, 2022.
- 755 Maasackers, J. D., Jacob, D. J., Sulprizio, M. P., Scarpelli, T. R., Nesser, H., Sheng, J.-X., Zhang, Y., Hersher, M., Bloom, A. A., Bowman, K. W., et al.: Global distribution of methane emissions, emission trends, and OH concentrations and trends inferred from an inversion of GOSAT satellite data for 2010–2015, *Atmospheric Chemistry and Physics*, 19, 7859–7881, <https://doi.org/10.5194/acp-19-7859-2019>, 2019.
- 760 Madrazo, J., Clappier, A., Belalcazar, L. C., Cuesta, O., Contreras, H., and Golay, F.: Screening differences between a local inventory and the Emissions Database for Global Atmospheric Research (EDGAR), *Science of the Total Environment*, 631, 934–941, <https://doi.org/10.1016/j.scitotenv.2018.03.094>, 2018.
- 765 Manjunath, K., Panigrahy, S., Kumari, K., Adhya, T., and Parihar, J.: Spatiotemporal modelling of methane flux from the rice fields of India using remote sensing and GIS, *International Journal of Remote Sensing*, 27, 4701–4707, <https://doi.org/10.1080/01431160600702350>, 2006.
- Martinez, A., Saunois, M., Poulter, B., Bousquet, P., Canadell, J. G., Jackson, R. B., Dlugokencky, E. J., Ciais, P., Bastviken, D., Blake, D. R., Castaldi, S., Etiope, G., Gedney, N., Höglund-Isaksson, L., Hugelius, G., Ito, A., Kleinen, T., Krummel, P. B., Liu, L., McDonald,

- 770 K. C., Melton, J. R., Müller, J., Murguia-Flores, F., Niwa, Y., Noce, S., Parker, R. J., Peng, C., Ramonet, M., Riley, W. J., Rosentreter, J. A., Segers, A., Smith, S. J., Tian, H., Tubiello, F. N., Tsuruta, A., Weber, T. S., Werf, G. R. v. d., Worthy, D., Yoshida, Y., Zhang, W., Zhang, Z., Zheng, B., Zhu, Q., Zhu, Q., and Zhuang, Q.: Supplemental data of the Global Carbon Project methane budget 2024 v1, 2024.
- 775 Metya, A., Datye, A., Chakraborty, S., Tiwari, Y. K., Sarma, D., Bora, A., and Gogoi, N.: Diurnal and seasonal variability of CO₂ and CH₄ concentration in a semi-urban environment of western India, *Scientific reports*, 11, 2931, <https://doi.org/10.1038/s41598-021-82321-1>, 2021.
- Miller, S. M. and Michalak, A. M.: Constraining sector-specific CO₂ and CH₄ emissions in the US, *Atmospheric Chemistry and Physics*, 17, 3963–3985, <https://doi.org/10.5194/acp-17-3963-2017>, 2017.
- Miller, S. M., Michalak, A. M., Detmers, R. G., Hasekamp, O. P., Bruhwiler, L. M., and Schwietzke, S.: China’s coal mine methane regulations have not curbed growing emissions, *Nature Communications*, 10, 303, <https://doi.org/10.1038/s41467-018-07891-7>, 2019.
- 780 Ministry of Environment, F. and Change, C.: India: First biennial update report to the United Nations framework convention on climate change, 2015.
- MoEFCC, .: India: Fourth Biennial update report to the United Nations Framework Convention on Climate Change, Ministry of Environment, Forest and Climate Change, Government of India., 2024.
- Montzka, S. A., Dlugokencky, E. J., and Butler, J. H.: Non-CO₂ greenhouse gases and climate change, *Nature*, 476, 43–50, <https://doi.org/doi:10.1038/nature10322>, 2011.
- 785 Myhre, G., Myhre, C. L., Samset, B., and Storelvmo, T.: Aerosols and their relation to global climate and climate sensitivity, *Nature Education Knowledge*, 4, 7, 2013a.
- Myhre, G., Shindell, D., Bréon, F.-M., Collins, W., Fuglestedt, J., Huang, J., Koch, D., Lamarque, J.-F., Lee, D., Mendoza, B., Nakajima, T., Robock, A., Stephens, G., Takemura, T., and Zhang, H.: Anthropogenic and natural radiative forcing, pp. 659–740, Cambridge University Press, Cambridge, UK, <https://doi.org/10.1017/CBO9781107415324.018>, 2013b.
- 790 Nisbet, E. G., Manning, M., Dlugokencky, E., Fisher, R., Lowry, D., Michel, S., Myhre, C. L., Platt, S. M., Allen, G., Bousquet, P., et al.: Very strong atmospheric methane growth in the 4 years 2014–2017: Implications for the Paris Agreement, *Global Biogeochemical Cycles*, 33, 318–342, <https://doi.org/10.1029/2018GB006009>, 2019.
- Palmer, P. I., Feng, L., Lunt, M. F., Parker, R. J., Bösch, H., Lan, X., Lorente, A., and Borsdorff, T.: The added value of satellite observations of methane for understanding the contemporary methane budget, *Philosophical Transactions of the Royal Society A*, 379, 20210 106, <https://doi.org/10.1098/rsta.2021.0106>, 2021.
- 795 Pandey, S., Gautam, R., Houweling, S., Van Der Gon, H. D., Sadavarte, P., Borsdorff, T., Hasekamp, O., Landgraf, J., Tol, P., Van Kempen, T., et al.: Satellite observations reveal extreme methane leakage from a natural gas well blowout, *Proceedings of the National Academy of Sciences*, 116, 26 376–26 381, <https://doi.org/10.1073/pnas.1908712116>, 2019.
- 800 Panigrahy, S., Upadhyay, G., Ray, S. S., and Parihar, J. S.: Mapping of cropping system for the Indo-Gangetic plain using multi-date SPOT NDVI-VGT data, *Journal of the Indian Society of Remote Sensing*, 38, 627–632, <https://doi.org/10.1007/s12524-011-0059-5>, 2010.

- Patra, P. K., Houweling, S., Krol, M., Bousquet, P., Belikov, D., Bergmann, D., Bian, H., Cameron-Smith, P., Chipperfield, M. P., Corbin, K., et al.: TransCom model simulations of CH₄ and related species: linking transport, surface flux and chemical loss with CH₄ variability in the troposphere and lower stratosphere, *Atmospheric Chemistry and Physics*, 11, 12 813–12 837, 2011.
- 805 Patra, P. K., Saeki, T., Dlugokencky, E. J., Ishijima, K., Umezawa, T., Ito, A., Aoki, S., Morimoto, S., Kort, E. A., Crotwell, A., et al.: Regional methane emission estimation based on observed atmospheric concentrations (2002–2012), *Journal of the Meteorological Society of Japan. Ser. II*, 94, 91–113, <https://doi.org/https://doi.org/10.2151/jmsj.2016-006>, 2016.
- Pillai, D., Buchwitz, M., Gerbig, C., Koch, T., Reuter, M., Bovensmann, H., Marshall, J., and Burrows, J. P.: Tracking city CO₂ emissions from space using a high-resolution inverse modelling approach: a case study for Berlin, Germany, *Atmospheric Chemistry and Physics*, 16, 9591–9610, <https://doi.org/10.5194/acp-16-9591-2016>, 2016.
- 810 Prather, M. J., Holmes, C. D., and Hsu, J.: Reactive greenhouse gas scenarios: Systematic exploration of uncertainties and the role of atmospheric chemistry, *Geophysical Research Letters*, 39, <https://doi.org/https://doi.org/10.1029/2012GL051440>, 2012.
- Qu, Z., Jacob, D. J., Shen, L., Lu, X., Zhang, Y., Scarpelli, T. R., Nesser, H., Sulprizio, M. P., Maasackers, J. D., Bloom, A. A., Worden, J. R., Parker, R. J., and Delgado, A. L.: Global distribution of methane emissions: a comparative inverse analysis of observations from the TROPOMI and GOSAT satellite instruments, *Atmospheric Chemistry and Physics*, 21, 14 159–14 175, <https://doi.org/10.5194/acp-21-14159-2021>, 2021.
- 815 Raju, A., Sijikumar, S., Valsala, V., Tiwari, Y. K., Halder, S., Girach, I., Jain, C. D., and Ratnam, M. V.: Regional estimation of methane emissions over the peninsular India using atmospheric inverse modelling, *Environmental Monitoring and Assessment*, 194, 647, <https://doi.org/10.1007/s10661-022-10323-1>, 2022.
- 820 Ramasamy, C. and Manivel, S.: An analysis of aspects of performance and difficulties of poultry farming in Namakkal, Tamilnadu, 2019.
- Rodgers, C. D.: *Inverse methods for atmospheric sounding: theory and practice*, vol. 2, World scientific, <https://doi.org/10.1142/3171>, 2000.
- Saunois, M., Bousquet, P., Poulter, B., Peregon, A., Ciais, P., Canadell, J. G., Dlugokencky, E. J., Etiope, G., Bastviken, D., Houweling, S., et al.: The global methane budget: 2000–2012, *Earth System Science Data Discussions*, 2016, 1–79, <https://doi.org/10.5194/essd-8-697-2016>, 2016.
- 825 Saunois, M., Stavert, A. R., Poulter, B., Bousquet, P., Canadell, J. G., Jackson, R. B., Raymond, P. A., Dlugokencky, E. J., Houweling, S., Patra, P. K., et al.: The global methane budget 2000–2017, *Earth System Science Data Discussions*, 2019, 1–136, <https://doi.org/10.5194/essd-12-1561-2020>, 2019.
- Saunois, M., Martinez, A., Poulter, B., Zhang, Z., Raymond, P., Regnier, P., Canadell, J. G., Jackson, R. B., Patra, P. K., Bousquet, P., et al.: Global methane budget 2000–2020, *Earth System Science Data Discussions*, 2024, 1–147, <https://doi.org/10.5194/essd-2024-115>, 2024.
- 830 Saunois, M., Martinez, A., Poulter, B., Zhang, Z., Raymond, P. A., Regnier, P., Canadell, J. G., Jackson, R. B., Patra, P. K., Bousquet, P., Ciais, P., Dlugokencky, E. J., Lan, X., Allen, G. H., Bastviken, D., Beerling, D. J., Belikov, D. A., Blake, D. R., Castaldi, S., Crippa, M., Deemer, B. R., Dennison, F., Etiope, G., Gedney, N., Höglund-Isaksson, L., Holgersson, M. A., Hopcroft, P. O., Hugelius, G., Ito, A., Jain, A. K., Janardanan, R., Johnson, M. S., Kleinen, T., Krummel, P. B., Lauerwald, R., Li, T., Liu, X., McDonald, K. C., Melton, J. R.,

- Mühle, J., Müller, J., Murguía-Flores, F., Niwa, Y., Noce, S., Pan, S., Parker, R. J., Peng, C., Ramonet, M., Riley, W. J., Rocher-Ros, G.,
835 Rosentreter, J. A., Sasakawa, M., Segers, A., Smith, S. J., Stanley, E. H., Thanwerdas, J., Tian, H., Tsuruta, A., Tubiello, F. N., Weber,
T. S., van der Werf, G. R., Worthy, D. E. J., Xi, Y., Yoshida, Y., Zhang, W., Zheng, B., Zhu, Q., Zhu, Q., and Zhuang, Q.: Global Methane
Budget 2000–2020, *Earth System Science Data*, 17, 1873–1958, <https://doi.org/10.5194/essd-17-1873-2025>, 2025.
- Scarpelli, T. R., Roy, E., Jacob, D. J., Sulprizio, M. P., Tate, R. D., and Cusworth, D. H.: Using new geospatial data and 2020 fossil
fuel methane emissions for the Global Fuel Exploitation Inventory (GFEI) v3, *Earth System Science Data Discussions*, 2025, 1–23,
840 <https://doi.org/10.5194/essd-2024-552>, 2025.
- Schaefer, H., Fletcher, S. E. M., Veidt, C., Lasseby, K. R., Brailsford, G. W., Bromley, T. M., Dlugokencky, E. J., Michel, S. E., Miller,
J. B., Levin, I., et al.: A 21st-century shift from fossil-fuel to biogenic methane emissions indicated by 13CH₄, *Science*, 352, 80–84,
[https://doi.org/DOI: 10.1126/science.aad2705](https://doi.org/DOI:10.1126/science.aad2705), 2016.
- Schneising, O.: Product User Guide (PUG) TROPOMI WFM-DOAS (TROPOMI/WFMD) XCH₄, [https://admin.climate.esa.int/media/
845 documents/PUG_CRDP9_v2_GHG-CCI_CH4_S5P_WFMD_v1.8.pdf](https://admin.climate.esa.int/media/documents/PUG_CRDP9_v2_GHG-CCI_CH4_S5P_WFMD_v1.8.pdf), 2024.
- Schneising, O., Buchwitz, M., Reuter, M., Heymann, J., Bovensmann, H., and Burrows, J. P.: Long-term analysis of carbon dioxide
and methane column-averaged mole fractions retrieved from SCIAMACHY, *Atmospheric Chemistry and Physics*, 11, 2863–2880,
<https://doi.org/https://doi.org/10.5194/acp-11-2863-2011>, 2011.
- Schneising, O., Buchwitz, M., Reuter, M., Bovensmann, H., Burrows, J. P., Borsdorff, T., Deutscher, N. M., Feist, D. G., Griffith, D. W., Hase,
850 F., et al.: A scientific algorithm to simultaneously retrieve carbon monoxide and methane from TROPOMI onboard Sentinel-5 Precursor,
Atmospheric Measurement Techniques, 12, 6771–6802, <https://doi.org/10.5194/amt-12-6771-2019>, 2019.
- Schneising, O., Buchwitz, M., Reuter, M., Vanselow, S., Bovensmann, H., and Burrows, J. P.: Remote sensing of methane leakage from
natural gas and petroleum systems revisited, *Atmospheric Chemistry and Physics*, 20, 9169–9182, [https://doi.org/10.5194/acp-20-9169-
2020](https://doi.org/10.5194/acp-20-9169-2020), 2020.
- 855 Schneising, O., Buchwitz, M., Hachmeister, J., Vanselow, S., Reuter, M., Buschmann, M., Bovensmann, H., and Burrows, J. P.: Advances
in retrieving XCH₄ and XCO from Sentinel-5 Precursor: improvements in the scientific TROPOMI/WFMD algorithm, *Atmospheric
Measurement Techniques*, 16, 669–694, <https://doi.org/https://doi.org/10.5194/amt-16-669-2023>, 2023.
- Sijkumar, S., Raju, A., Valsala, V., Tiwari, Y., Girach, I., Jain, C. D., and Ratnam, M. V.: High-Resolution Bayesian Inversion of Carbon
Dioxide Flux Over Peninsular India, *Atmospheric Environment*, 308, 119 868, <https://doi.org/10.1016/j.atmosenv.2023.119868>, 2023.
- 860 Skamarock, W. C., Klemp, J. B., Dudhia, J., Gill, D. O., Barker, D. M., Duda, M. G., Huang, X., Wang, W., and Powers, J. G.: A description of
the advanced research WRF, National Center for Atmospheric Research, Boulder, CO), Version, 3, <https://doi.org/10.5065/D68S4MVH>,
2008.
- Skeie, R. B., Hodnebrog, Ø., and Myhre, G.: Trends in atmospheric methane concentrations since 1990 were driven and modified by anthro-
pogenic emissions, *Communications Earth & Environment*, 4, 317, <https://doi.org/10.1038/s43247-023-00969-1>, 2023.

- 865 Solazzo, E., Crippa, M., Guizzardi, D., Muntean, M., Choulga, M., and Janssens-Maenhout, G.: Uncertainties in the Emissions Database for Global Atmospheric Research (EDGAR) emission inventory of greenhouse gases, *Atmospheric Chemistry and Physics*, 21, 5655–5683, <https://doi.org/10.5194/acp-21-5655-2021>, 2021.
- Stevenson, D. S., Zhao, A., Naik, V., O’connor, F. M., Tilmes, S., Zeng, G., Murray, L. T., Collins, W. J., Griffiths, P. T., Shim, S., et al.: Trends in global tropospheric hydroxyl radical and methane lifetime since 1850 from AerChemMIP, *Atmospheric Chemistry and Physics*, 870 20, 12 905–12 920, <https://doi.org/https://doi.org/10.5194/acp-20-12905-2020>, 2020.
- Stocker, T. F., Qin, D., Plattner, G., Tignor, M., Allen, S., Boschung, J., Nauels, A., Xia, Y., Bex, V., Midgley, P., et al.: Contribution of working group I to the fifth assessment report of the intergovernmental panel on climate change, *Climate change*, 5, 1–1552, <https://doi.org/10.1017/CBO9781107415324.004>, 2013.
- Survey of India: Political map of India, <https://www.surveyofindia.gov.in/pages/political-map-of-india>, accessed on: 21 May 2024, 2024.
- 875 Thilakan, V., Pillai, D., Gerbig, C., Galkowski, M., Ravi, A., and Anna Mathew, T.: Towards monitoring CO₂ source-sink distribution over India via inverse modelling: Quantifying the fine-scale spatiotemporal variability of atmospheric CO₂ mole fraction, *Atmospheric Chemistry and Physics Discussions*, 2022, 1–38, <https://doi.org/10.5194/acp-22-15287-2022>, 2022.
- Thompson, R. L., Montzka, S. A., Vollmer, M. K., Arduini, J., Crotwell, M., Krummel, P. B., Lunder, C., Mühle, J., O’doherly, S., Prinn, R. G., et al.: Estimation of the atmospheric hydroxyl radical oxidative capacity using multiple hydrofluorocarbons (HFCs), *Atmospheric* 880 *Chemistry and Physics*, 24, 1415–1427, 2024.
- Turner, A., Jacob, D. J., Wecht, K. J., Maasackers, J. D., Lundgren, E., Andrews, A. E., Biraud, S. C., Boesch, H., Bowman, K. W., Deutscher, N. M., et al.: Estimating global and North American methane emissions with high spatial resolution using GOSAT satellite data, *Atmospheric Chemistry and Physics*, 15, 7049–7069, <https://doi.org/10.5194/acp-15-7049-2015>, 2015.
- Uma, K., Girach, I. A., Chandra, N., Patra, P. K., Kumar, N. K., and Nair, P. R.: CO₂ variability over a tropical coastal station in India: 885 Synergy of observation and model, *Science of The Total Environment*, 957, 177 371, <https://doi.org/10.1016/j.scitotenv.2024.177371>, 2024.
- Vellalassery, A., Pillai, D., Marshall, J., Gerbig, C., Buchwitz, M., Schneising, O., and Ravi, A.: Using TROPOspheric Monitoring Instrument (TROPOMI) measurements and Weather Research and Forecasting (WRF) CO modelling to understand the contribution of meteorology and emissions to an extreme air pollution event in India, *Atmospheric Chemistry and Physics*, 21, 5393–5414, <https://doi.org/10.5194/acp-21-5393-2021>, 2021.
- 890 Wang, Y., Yuan, Q., Li, T., Yang, Y., Zhou, S., and Zhang, L.: Seamless mapping of long-term (2010–2020) daily global XCO₂ and XCH₄ from the Greenhouse Gases Observing Satellite (GOSAT), Orbiting Carbon Observatory 2 (OCO-2), and CAMS global greenhouse gas reanalysis (CAM5-EGG4) with a spatiotemporally self-supervised fusion method, *Earth System Science Data*, 15, 3597–3622, <https://doi.org/10.5194/essd-15-3597-2023>, 2023.
- 895 Wilcox, R.: *Trimming and Winsorization*, John Wiley Sons, Ltd, <https://doi.org/10.1002/0470011815.b2a15165>, 2005.

- Yokota, T., Yoshida, Y., Eguchi, N., Ota, Y., Tanaka, T., Watanabe, H., and Maksyutov, S.: Global concentrations of CO₂ and CH₄ retrieved from GOSAT: First preliminary results, *Sola*, 5, 160–163, <https://doi.org/10.2151/sola.2009-041>, 2009.
- Zhang, X., Lee, X., Griffis, T. J., Baker, J. M., and Xiao, W.: Estimating regional greenhouse gas fluxes: an uncertainty analysis of planetary boundary layer techniques and bottom-up inventories, *Atmospheric chemistry and physics*, 14, 10705–10719, <https://doi.org/10.5194/acp-14-10705-2014>, 2014.
- Zhang, Y., Jacob, D. J., Lu, X., Maasakkers, J. D., Scarpelli, T. R., Sheng, J.-X., Shen, L., Qu, Z., Sulprizio, M. P., Chang, J., Bloom, A. A., Ma, S., Worden, J., Parker, R. J., and Boesch, H.: Attribution of the accelerating increase in atmospheric methane during 2010–2018 by inverse analysis of GOSAT observations, *Atmospheric Chemistry and Physics*, 21, 3643–3666, <https://doi.org/10.5194/acp-21-3643-2021>, 2021.
- 905 Zhou, L., Warner, J., Nalli, N. R., Wei, Z., Oh, Y., Bruhwiler, L., Liu, X., Divakarla, M., Pryor, K., Kalluri, S., et al.: Spatiotemporal variability of global atmospheric methane observed from two decades of satellite hyperspectral infrared sounders, *Remote Sensing*, 15, 2992, 2023.